Journal of Materials Research and Technology 45 (2026) 6223–6239

Contents lists available at ScienceDirect

Journal of Materials Research and Technology

journal homepage: www.elsevier.com/locate/jmrt

Morphological control of copper edge-tails via mass-transfer loading toward enhanced thermo-mechanical reliability of power module substrates

Hoonhee Jang [a], Hyemin An [a], Sangyeun Park [b], Hongyun So [a,b,*]

[a] Department of Semiconductor Engineering, Hanyang University, Seoul, 04763, South Korea
[b] Department of Mechanical Engineering, Hanyang University, Seoul, 04763, South Korea

ARTICLE INFO

Keywords:
Wet etching
Loading effect
Dummy pattern
Direct bonded copper (DBC) substrate
Level-set simulation

ABSTRACT

The thermal cycling reliability of direct bonded copper (DBC) substrates depends on the edge geometry of the etched copper patterns, and a long, low-angle edge tail extends the fatigue life. Existing geometry-control techniques, however, require additional lithography and multistep etching. This study achieved quantitative edge-tail control in a single wet-etching step by inducing a loading effect with dummy mask patterns. Etching all 49 combinations of dummy width w and gap s on 300 μm copper yielded a morphology regime map with a single-continuous-tail process window. A topology-capable diffusion-reaction level-set simulator reproduced dummy detachment and the final cross-sections of 12 holdout conditions with a median root-mean-square error (RMSE) of 10.2 μm. The simulated fields gave a dimensionless loading law in terms of the supply constriction d/s and the reaction load w/d, whose exponents are consistent with a one-dimensional diffusion-channel model. The measured tail length followed a mask-only design equation that scales with $\sqrt{s \cdot w}$, and the dummy-removability boundary predicted without tuning, 428 ± 24 μm, exceeds the measured 350–400 μm by less than one mask step. A thermo-mechanical finite-element analysis of the measured profiles showed that every design-window tail lowers the cyclic copper plastic strain and the ceramic edge stress relative to dummy-free references, corresponding to a 1.6–3.6-fold relative fatigue-life estimate. Within the window ($w \leq 200$ μm, $s \leq 350$ μm), these results provide a mask-only route from the mask geometry to the complete edge profile that is applicable to industrial DBC patterning and transferable to other copper thicknesses after recalibration.

Nomenclature

Latin symbols	
$A(n)$	Directional anisotropy factor of the etch rate (−)
C	Prefactor of the dimensionless loading law, Eq. (8) (−)
C_{Bulk}	Bulk oxidant concentration (mol/m^3)
D	Effective diffusion coefficient of the dissolved species (m^2/s)
K_{inh}	Etch inhibition constant (m^3/mol)
L	Edge-tail length (m)
L_0	Tail length of the dummy-free reference (m)
LF	Loading factor, ratio of gap to reference-plane etch depth (−)
a_h	Intrinsic horizontal-to-vertical anisotropy of etching (−)
c_e	Oxidant (Fe^{3+}) concentration (mol/m^3)
c_p	Product (Cu^{2+}) concentration (mol/m^3)
d	Copper layer thickness (m)
$f(\xi)$	Master-curve shape function of the tail (−)
f_{inh}	Etch inhibition function of the product concentration (−)

(*continued on next column*)

(*continued*)

$h(x)$	Digitized copper surface profile (m)
k	Coefficient of the tail-length design equation, Eq. (9) (−)
k_s	Surface reaction rate constant (m/s)
s	Gap (opening) width between the dummy and the main PR (m)
t_{wc}	Punch-through time of the wide opening (s)
v_n	Normal velocity of the etch front (m/s)
w	Dummy pattern width (m)
w^*	Dummy-removability boundary width (m)
Greek symbols	
β_p	Coefficient of the aspect-ratio transport closure (−)
δ_{BL}	Bulk Dirichlet offset on the Nernst-layer scale (m)
η_{eff}	Effective undercut ratio, lateral undercut over vertical etch depth (−)
Δ^*	Offset of the common comparison time from t_{wc} (s)
$\Delta\varepsilon_p$	Equivalent plastic strain per cycle in the copper, band-averaged (−)
σ_1	Maximum first principal stress in the ceramic, band-averaged (Pa)
θ_1	Toe angle of the tail at the substrate contact (°)

(*continued on next page*)

* Corresponding author. Department of Semiconductor Engineering, Hanyang University, Seoul, 04763, South Korea.
E-mail address: hyso@hanyang.ac.kr (H. So).

https://doi.org/10.1016/j.jmrt.2026.10.134
Received 7 August 2026; Received in revised form 2 October 2026; Accepted 13 October 2026
Available online 14 October 2026
2238-7854/© 2026 The Authors. Published by Elsevier B.V. This is an open access article under the CC BY-NC-ND license (http://creativecommons.org/licenses/by-nc-nd/4.0/).

(*continued*)

ξ	Normalized horizontal coordinate x/L (−)
φ	Level-set function (m)
Abbreviations	
AMB	Active metal brazing
DBC	Direct bonded copper
FE	Finite element
FR-4	Flame-retardant grade 4 glass-epoxy laminate
OM	Optical microscopy
PR	Photoresist
RMSE	Root-mean-square error

1. Introduction

Power electronic modules are increasingly used in harsh environments such as electric vehicles, aviation, and renewable energy systems, where the reliability of the insulating substrate largely determines the module lifetime [1]. Direct bonded copper (DBC) substrates, in which copper foils several hundred micrometers thick are bonded to both faces of a ceramic layer and the upper copper is patterned by wet etching, are widely used owing to their high thermal conductivity and dielectric strength [2]. Table 1 compares the ceramics used for power-module substrates. Al_2O_3 is the most widely used for cost reasons, whereas AlN and Si_3N_4 offer a higher thermal conductivity and a higher fracture toughness, respectively, and all of them are patterned by the same copper wet-etching step, so the edge-geometry control developed here is not specific to one ceramic. Under thermal cycling between −55 and 150 °C, the mismatch in the coefficient of thermal expansion (CTE) between copper and ceramic causes stress and plastic deformation to accumulate at the interface [3], and the etched pattern edges act as geometric singularities at which cracks initiate and propagate into the ceramic [4,5].

Geometry-control techniques such as edge tails, dimples, stepped edges, and ladder-type copper layers have therefore been investigated to mitigate this stress concentration [8,10,11]. A 0.5 mm edge tail, which blunts the corner singularity, more than doubles the thermal cycling lifetime [10], and a ladder-type structure extends it approximately threefold [8]. Lifetime models that treat crack initiation and propagation jointly have confirmed experimentally that a stepped copper edge substantially extends the fatigue life of Al_2O_3-DBC [12], and failure analyses have identified the copper edge as the crack initiation site, with the crack deflection into the ceramic governed by the interface stress intensity [13]. Recent studies have extended this geometry-reliability link to the layout of the back-side copper [14] and to data-driven optimization of the notch geometry at the copper edge [15], while in-situ strain measurements on Si_3N_4-AMB substrates [16] and Chaboche-based lifetime estimates [17] have quantified the cyclic plastic strain of the copper that drives this failure.

These studies, however, identify geometries that improve the lifetime without controlling them as a design variable. The edge-tail study demonstrated the lifetime gain of a 0.5 mm tail but did not report how the etch sets the tail geometry, and the dimple, stepped, and ladder-type approaches require additional lithography and multistep etching, so realizing such geometries within a single etching process remains an open challenge. Obtaining a target structure directly from the fabrication route is a recurring objective in materials processing [18].

Research on the etched geometry itself has developed through coupled diffusion-reaction models. Kuiken showed that the front advance in diffusion-controlled wet etching is set by the mass transfer of the reactive species [19], and Georgiadou and Alkire showed for copper etching in acidic chloride solutions that local mass transfer governs the etch rate and anisotropy and that product supersaturation inside a cavity suppresses etching [20–22]. This is the same mechanism as the loading effect, in which the local pattern density changes the balance between reactant consumption and product accumulation. In dry etching, the loading effect and the aspect-ratio dependence are well established [23–25], but dummy patterns are used there to suppress geometric variation rather than to synthesize a target cross-section. Turning the loading effect into a shape-design variable requires the local concentration field, which cannot be measured and must be obtained from a validated simulation. For thick copper, this is difficult, because the merging of the etch fronts beneath the dummy and the detachment of the dummy are topology changes that conventional mesh-based moving-boundary analyses cannot handle.

This study therefore deliberately induces the loading effect with dummy patterns to form and control a long, gentle edge tail in a single wet-etching step through the mask design alone. The central hypothesis is that a dummy of width w placed at a gap s beside the main pattern edge depletes the reactant in the narrow gap and slows the local etching, and that the edge develops into an elongated tail through the merging and detachment of the undercuts beneath the dummy. Two phenomena long regarded as defects in wet etching are thus used as resources: the isotropic undercut as the geometric source of the detachment and of the taper, and the loading effect as the control variable. The resulting taper weakens the stress singularity of a sharp re-entrant corner [26] and lowers the electric field peak at the ceramic-metal-encapsulant triple point [27]. Prior work has thus established that the geometric relaxation of the copper edge governs the interfacial stress and the fatigue life [8,10,11,13], and the question addressed here is how such a geometry can be realized reproducibly and predicted quantitatively within a single etch. For a copper thickness of $d = 300$ μm, the study proceeds in five steps, namely (i) a morphology regime map from 56 optical microscopy (OM) cross-sections covering all 49 combinations of w and s, (ii) a two-dimensional diffusion-reaction level-set simulator that handles topology changes and is tested against the cross-sections of holdout conditions, (iii) a dimensionless loading law derived from the simulated fields and a mask-only design equation for the tail length derived from the measurements, (iv) a design procedure that predicts the entire cross-section and the dummy-removability boundary from the mask geometry, and (v) a thermo-mechanical finite-element analysis of the measured profiles relative to dummy-free references.

The novelty of this work relative to the state of the art lies in four points. First, whereas the edge-tail, dimple, stepped, and ladder-type approaches [8,10,11] treat the tail length as an input to finite-element analysis or require additional lithography and multistep etching, the present method realizes the tail with a single lithography step and a single etch, with the two mask dimensions (w, s) as the only design variables. Second, whereas dummy patterns have been used to suppress non-uniformity caused by the pattern density [23–25], the loading effect is converted here into a shape-design variable, and the tail length obeys

Table 1
Representative properties of ceramic substrates used in power modules and of the copper metallization. The CTE, flexural strength, and fracture toughness of the ceramics are taken from Ref. [6], and the CTEs of 96% Al_2O_3 and copper are taken from Refs. [7] and [8], respectively. The thermal conductivities are those of commercial substrates reported in Refs. [7,9]. DBC denotes direct bonded copper, and AMB denotes active metal brazing.

Ceramic	CTE (10^{-6} K^{-1})	Thermal conductivity (W m^{-1} K^{-1})	Flexural strength (MPa)	Fracture toughness (MPa $m^{0.5}$)	Metallization process
Al_2O_3 (96%)	6.8–8	25	300–400	3.5–4.0	DBC
AlN	4.6	170–190	220–310	3.0–3.5	DBC/AMB
Si_3N_4	2.7–3.4	60–90	600–750	6.5–7.5	AMB
Cu (metallization, for reference)	16.4–17	—	—	—	—

the measurement-based design equation $L = L_0 + 0.74\sqrt{s \cdot w}$ with $R^2 = 0.83$, while the entire profile follows a single master curve. Third, whereas the diffusion-reaction models of copper etching [19–22] and recent coupled flow-etching simulations [28] treat a single cavity or opening of fixed topology, the topology-capable simulator developed here reproduces dummy detachment and the final cross-sections of holdout conditions with a median root-mean-square error (RMSE) of 10.2 μm and predicts, without tuning, a dummy-removability boundary of 428 ± 24 μm, less than one mask step above the measured 350–400 μm. Fourth, the reliability implication of the realized geometry is quantified rather than inferred, because a finite-element analysis of the measured profiles gives a 1.6–3.6-fold relative fatigue-life estimate against dummy-free references. Unlike recent studies that optimize the edge geometry by finite-element and machine-learning search [15] or the layout of the back-side copper [14] without addressing how the geometry is produced, and unlike wet-etching simulations of an isolated opening [28], the present work links the mask design, the etched geometry, and its thermo-mechanical implication in one framework, and Section 4.7 compares these approaches in detail. Section 2 describes the specimens, Section 3 the simulator, Section 4 the results, and Section 5 the conclusions.

2. Methods

2.1. Sample preparation

Because the supply of actual DBC substrates was limited, custom-made substrates consisting of 300 μm thick copper foil laminated on an FR-4 base were used. Both FR-4 and ceramic are inert and impermeable to Fe^{3+} and Cu^{2+} and enter Eqs. (1)–(3) only as a no-flux boundary, so the support substrate does not participate in the formation of the edge geometry. Differences in foil microstructure appear primarily in the absolute etch rate, which is absorbed into the rate constant k_s. A uniform shift in the rate scale mainly shifts the process timeline, which the event-anchored readouts of Section 3.3 absorb to first order. The copper thickness of 300 μm corresponds to that of the upper copper layer of commercial DBC substrates. One caveat lies outside the scope of the transport argument. The copper in a bonded DBC substrate is recrystallized during high-temperature bonding, and the grain structure and grain-boundary etching can influence the intrinsic anisotropy a_h and the fine morphology of the tail toe. The transport-side framework of Eqs. (8)–(10) and (13) is independent of the support, whereas the near-isotropic a_h adopted for the present rolled foil should be re-verified when the method is applied to bonded DBC copper.

The etching patterns were defined by photolithography using the mask shown in Fig. 1a. Fig. 1b shows the overall process, which proceeded as follows: spin coating, soft baking, exposure, development, and etching. After cleaning and drying, a negative-tone photoresist (PR, THB-151N) was spin-coated at 2000 rpm for 30 s to obtain a thickness of approximately 25 μm, followed by soft baking at 130 °C for 11 min.

The soft-baked specimens were exposed through the designed mask using a mask aligner (MDA-400M, MIDAS SYSTEM Co., Ltd.) for 110 s (≈2.3 J/cm^2). The mask consisted of a total of 49 patterns combining two design variables: the dummy width w (100–400 μm) adjacent to the main PR edge and the gap width s (100–400 μm) between the dummy and the main PR (denoted as the opening width s in the figures). The total etching opening width, measured from the main PR edge to the opposite boundary, was fixed at 2000 μm. This width is much larger than w and s (100–400 μm), so the central region of the opening acts as a stable mass-transfer reference plane unaffected by the loading effect. The exposed specimens were then developed by immersion in a developer solution for 10 min.

Subsequently, the specimens were wet etched. A ferric chloride ($FeCl_3$)-based solution was used as the etchant, with a composition of approximately 40 wt% anhydrous $FeCl_3$ ($C_{Bulk} \approx 3.5 \times 10^3$ mol/m^3 based on a density of ≈ 1.42 g/mL), approximately 1 wt% HCl, and the balance water. In $FeCl_3$ solutions, copper dissolves through the oxidation reaction $Cu + 2FeCl_3 \rightarrow CuCl_2 + 2FeCl_2$, and the reaction rate is known to be largely controlled by mass transfer, that is, by the supply of the oxidant (Fe^{3+}) to the surface and the removal of the product (Cu^{2+}) [29,30]. Etching was performed by immersion at a solution temperature of 40 °C with 40 rpm agitation by an orbital shaker. Compared with production spray etching, immersion with orbital agitation has simpler mass-transfer boundary conditions, which makes it suitable for isolating the mask-induced local loading from flow disturbances. The total etching time was 2.5 h, which coincided with the time at which the vertical front of the wide opening reached the substrate, denoted t_{wc} in Section 4.3, and no separate over-etch period was applied. Because one orbital period is much shorter than the etching time and the patterns are far smaller than the orbital diameter, the time-averaged mass transfer has no azimuthal bias, which is consistent with the left-right symmetric boundary condition and the isotropic mixing term of Eq. (2) in Section 3.2. After etching was complete, the specimens were rinsed with deionized water, dried, and stripped of the residual PR. To track the evolution of the front shape, specimens of identical design were withdrawn at 30 min intervals between 30 and 150 min and sectioned separately.

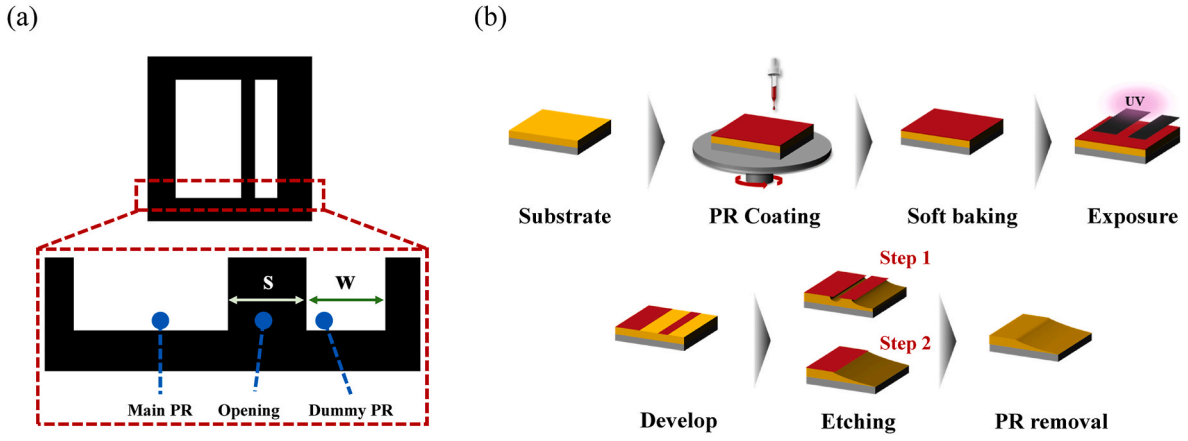


Fig. 1. (a) Photomask defining the main PR, the opening s, and the dummy PR width w. (b) Schematic of the fabrication process. A PR layer is first spin-coated onto the substrate and soft-baked, after which the pattern is defined by UV exposure and development. The exposed metal is then removed by $FeCl_3$ wet etching. As the etching proceeds, the underlying metal is initially removed (Step 1), and the dummy PR is subsequently detached once its supporting metal is undercut (Step 2). Finally, the remaining PR is stripped to complete the process.

2.2. Characterization and image digitization

After etching, the specimens were sectioned, polished (NA-P2001N, Nanotech, using SiC #2000/#3000 papers at 100–200 rpm), and observed under an optical microscope (BX53M, Olympus). A total of 56 cross-sectional images were acquired from the final specimens, comprising 49 images covering all dummy (*w, s*) combinations and seven dummy-free references. The combination-wise inventory is presented with the regime map in Section 4.1. Repeatability under identical conditions was assessed using seven specimens fabricated under the dummy-free reference condition, and their tail lengths (189–205 μm) exhibited a standard deviation of 6.6 μm, which was used as the representative reproducibility uncertainty of the measured tail length *L*.

The acquired OM cross-sections were digitized using a custom Python script to extract the edge profiles for quantitative comparison with the simulation. For each image, contour extraction and positional alignment to the main PR edge were performed, as illustrated in Fig. 2a, to convert the profiles into numerical curves *h(x)* in a common coordinate system, where the tail length *L* is defined as the horizontal distance from the onset of the undercutting beneath the main PR to the substrate contact point. The metric definitions are shown in Fig. 2b. The dataset of 56 profiles aligned in the common coordinate system served as a shared basis for regime classification, shape validation, and master-curve analysis.

3. Level-set simulation of the etching process

3.1. Modeling approach

The present analysis adopts a two-dimensional diffusion-reaction level-set formulation because the central event of this problem is a topological change at the interface. Specifically, the etching fronts on both sides merge beneath the dummy, after which the unsupported dummy PR detaches, and cusps form and are subsequently annihilated at the tip of the tail. Moving-boundary techniques that track the interface explicitly, such as deformed-geometry or arbitrary Lagrangian–Eulerian (ALE) methods, suffer from element self-intersection when fronts merge and in principle cannot handle such topology changes [31]. The formulation of Georgiadou and Alkire considers only a single cavity.

The level-set method represents the interface implicitly as the zero-level set of a signed distance function on a background grid. Front merging, splitting, and cusp formation are therefore handled naturally as topology changes of the function, and a correct propagation that satisfies the entropy condition is guaranteed even at the cusps [32,33]. Applications of the method to etching and deposition [34] and to wet etching [35] have also been reported. The phase-field method [36,37], another topology-capable approach, must resolve the thickness of the diffuse interface on the grid, which is costly for a 300 μm copper layer, whereas the level-set method maintains a sharp interface whose velocity is determined directly by the quantities of Eq. (4).

3.2. Governing equations

Wet etching is a mass-transfer-mediated process in which the oxidant diffuses to and reacts with the copper surface, and the reaction products are discharged back into the bulk [19,22,29]. In the present system, the bulk-exposed reference plane lies in a mixed-control regime, whereas transport limitation develops selectively within the loading-affected gap. The target reaction is the oxidative dissolution $Cu + 2Fe^{3+} \rightarrow Cu^{2+} + 2Fe^{2+}$, which is rate-limited by oxidant supply and product removal. The model therefore solves the two-species transport of the oxidant concentration c_e and the product concentration c_p, with the surface receding at a rate set by the local surface concentrations, and the transport is governed by diffusion and agitation-induced mixing.

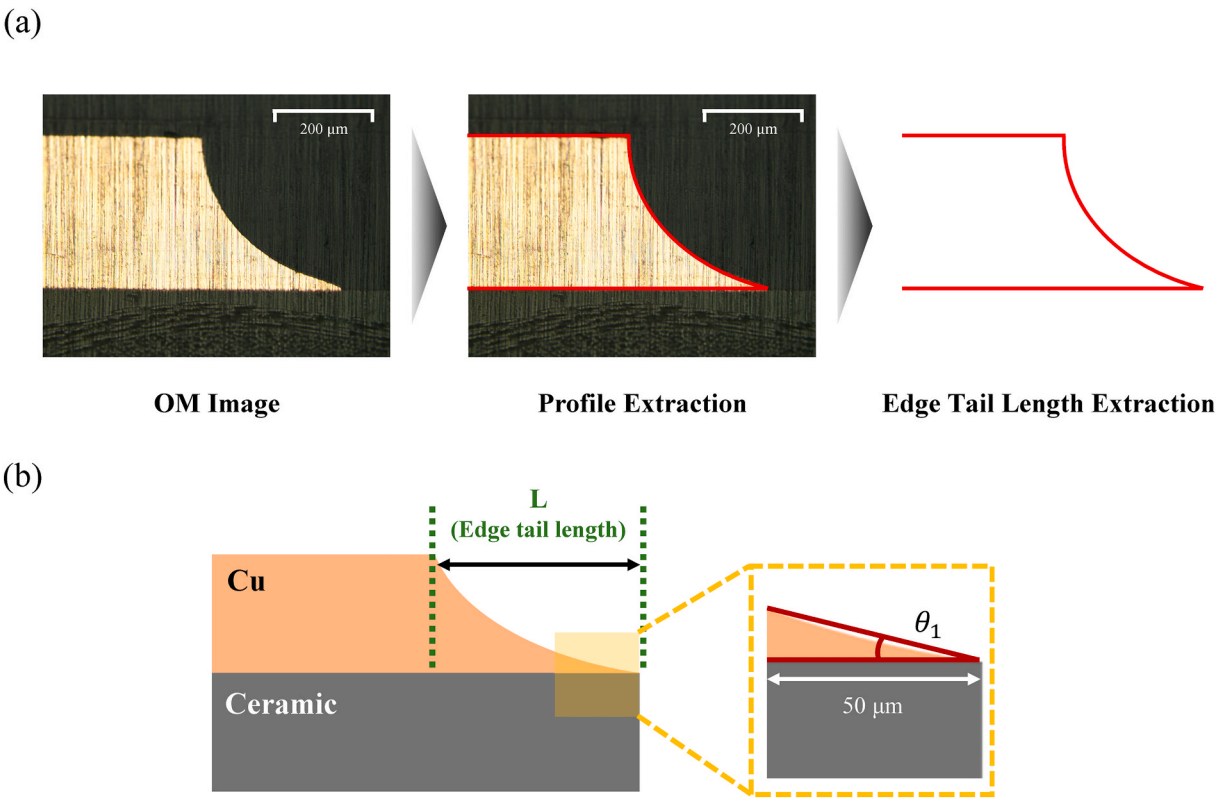


Fig. 2. Edge-tail metrics from cross-sectional profiles. (a) Extraction procedure, in which the OM image is first converted into a digitized Cu profile *h(x)*, from which the edge-tail length is subsequently obtained. (b) Definitions. The tail length *L* is the horizontal distance from the main-PR corner to the substrate contact point, and the toe angle θ_1 is the slope over a 50 μm chord at the contact point, which is taken as the first crossing of $h = 2$ μm with linear interpolation.

$$\frac{\partial c}{\partial t} + \nabla\cdot(-D\nabla c) = R, \left(c = c_e, c_p\right) \tag{1}$$

Here, D denotes the diffusion coefficient of each species. Measured literature values at 298 K are $D_p = 1.28 \times 10^{-9}$ m^2/s for the product (Cu^{2+}) [38] and $D_e \approx 0.60 \times 10^{-9}$ m^2/s for the oxidant (Fe^{3+}) [39]. Correcting these values to the process temperature of 40 °C (313 K) with the Stokes–Einstein relation, $D \propto T/\mu$, which accounts for the temperature dependence of the viscosity of water, gives approximately 1.83×10^{-9} m^2/s and 0.86×10^{-9} m^2/s, respectively. The present analysis uses a common effective diffusion coefficient $D = 1.2 \times 10^{-9}$ m^2/s for both species. Hereafter, $D_e = D_p = D$, and the effective value on the product side is locally reduced by the aspect-ratio (AR) closure described below. This value lies between the two corrected literature values, and because the absolute rate scale is absorbed into k_s, which is anchored to the measured etch rate at 40 °C, this choice mainly affects the timeline rather than the geometry. Forced convection due to agitation was approximated by the volumetric mixing term R instead of resolving the flow field directly. As discussed in Section 2.1, the time-averaged orbital flow has no azimuthal bias, which justifies this isotropic mixing-term approximation and the assumption of left-right symmetry.

$$R_e = K_{MIX}(C_{Bulk} - c_e), R_p = -K_{MIX}c_p \tag{2}$$

Here, C_{Bulk} is the oxidant concentration of the bulk solution (3530 mol/m^3), and K_{MIX} is the mixing rate constant. In the production calculations, this mixing term was implemented in the limit $K_{MIX} \to \infty$ as an interface-tracking Dirichlet constraint that fixes the liquid lying farther from the solid surface than a local boundary-layer thickness δ_{local} at the bulk values $c_e = C_{Bulk}$ and $c_p = 0$. Here, δ_{local} is an uncalibrated fixed parameter on the scale of the Nernst diffusion layer, with a default of $\delta_{BL} = 100$ μm and a lower bound of 50 μm above residual peaks. In this limit, K_{MIX} drops out of the formulation. The finite-rate form of Eq. (2) is retained as a general statement into which the agitation condition is incorporated, and this general form underpins the transferability argument presented in Section 5. The lateral and bottom boundaries are no-flux boundaries. The bath volume was large relative to the total amount of oxidant consumed, and the bulk concentration C_{Bulk} was therefore treated as constant, an assumption that affects the absolute timeline rather than the geometry. The mixing term was applied only to the bulk region above the openings. Inside the openings, only diffusion is effective, so the supply-removal balance varies with the opening width and the etch rate becomes position dependent. The loading effect is thereby reproduced self-consistently through the same mass-transfer process as the product-accumulation mechanism in the cavities of Georgiadou and Alkire.

At the copper surface where etching occurs (the $\varphi = 0$ level set), the oxidant is consumed by a first-order reaction, and the product is released according to the stoichiometry of the above reaction.

$$-n\cdot(-D_e\nabla c_e) = -k_s c_e, -n\cdot\left(-D_p\nabla c_p\right) = \frac{k_s c_e}{2} \tag{3}$$

Here, k_s is the surface reaction rate constant, and n is the unit normal vector pointing outward from the computational domain. The Damköhler number $Da = k_s d/D$, defined with the anchored k_s and the copper thickness d as the characteristic length, is approximately 1.0 under the present conditions. Etching of the bulk-exposed reference plane therefore lies in a mixed-control regime in which the surface reaction and the diffusive supply are comparable. Here, k_s is an effective constant that absorbs unresolved near-interface transport such as micro-convection. In the narrow gap between the dummy and the main PR, by contrast, the effective diffusion path lengthens and the reaction load accumulates as the etching deepens. Consequently, the dimensionless group $Da_z\left(1 + \frac{c_1 w}{s}\right)$ that governs the local suppression exceeds unity, and mass-transfer limitation develops selectively where the loading acts. Here, Da_z is the local Damköhler number with the etch depth z as the length scale, and $\left(1 + \frac{c_1 w}{s}\right)$ represents the reaction load imposed by the dummy, with c_1 an order-one geometric constant. Mass-transfer dominance is thus not a global constant but a local phenomenon created by the opening geometry. Oxidant diffusion, product removal, and surface kinetics act as follows. Under mixed control on the reference plane, the etch rate is set jointly by the surface kinetics k_s and the locally available oxidant, and the cavity retains the near-isotropic shape dictated by $A(n)$. Once the gap becomes transport limited, the rate is capped by the oxidant flux that can diffuse through the gap and is further reduced by product accumulation through the inhibition function of Eq. (5). The gap floor therefore lags behind the reference plane, and the merged front starts from a shallower, laterally offset geometry, which ultimately lengthens the tail. Oxidant supply and product removal share the same diffusion path and thus scale together with the gap aspect ratio, whereas the surface kinetics enters only through k_s and the Damköhler ratio. The first-order assumption in Eq. (3) is thus valid as a linear response to the local supply flux, and the geometry is determined by the concentration field rather than by the details of the reaction. In proportion to the amount of copper consumed by the reaction, the surface recedes at a normal velocity v_n.

$$v_n = \frac{M_{Cu}k_s c_e}{2\rho_{Cu}}\cdot f_{inh}\left(c_p\right)\cdot A(n), \tag{4}$$

where M_{Cu} and ρ_{Cu} are the molar mass and the density of Cu, respectively. f_{inh} is the etch inhibition function, which represents the slowing of the reaction as the local product concentration increases. Its functional form is a smooth first-order inhibition that approximates, to leading order, the threshold-type mechanism of product supersaturation and salt film formation. In a comparison with a threshold-type alternative, the topological events and the detachment time (±11%) were preserved, whereas the tail length changed by 17%–21%. This sensitivity concerns the position of the tail terminus, whereas the cross-sectional RMSE in Section 4.2 is a full-profile metric, so the two results are consistent.

$$f_{inh}\left(c_p\right) = \frac{1}{1 + K_{inh}c_p} \tag{5}$$

$A(n)$ is a directional factor that represents the intrinsic anisotropy of etching, $A(n) = (n_y^2 + a_h^2 n_x^2)^{1/2}$, which takes the value of 1 in the vertical direction and a_h in the horizontal direction and is applied in the advection step. a_h was fixed at 0.986, a near-isotropic input, and was not adjusted thereafter. Varying a_h over 0.98–1.00 did not significantly change the geometry or the ordering across conditions. In addition, an aspect-ratio closure that represents the unresolved transport resistance of narrow openings was applied to the product transport, $D_{p,eff} = D_p/(1 + \beta_p \cdot AR)$, where AR is the local ratio of the etch depth to the width of the opening at the PR level and is updated upon detachment. This term is a semi-empirical closure of the same origin as the aspect-ratio-conductance scaling of dry etching [23,25], and $\beta_p = 2.0$ was selected during the model development described in Section 3.3. The shape evolution of the copper surface is tracked on the background grid by the advection equation of the level-set function φ, which is negative in the copper and positive in the etchant [33,40].

$$\frac{\partial \varphi}{\partial t} - v_n|\nabla\varphi| = 0 \tag{6}$$

Overall, the loading effect arises from the coupling of two-species transport and surface reactions, supplemented by the closures described above. The parameters are listed in Table 2.

3.3. Numerical implementation, calibration, and verification

The computational domain was constructed as a two-dimensional cross-section that includes the main PR, the dummy pattern, and the

Table 2
Physical properties and numerical parameters used in the level-set simulation.

Parameter	Symbol	Value	Source
Cu layer thickness	d	300 μm	Measured
Bulk oxidant concentration	C_{Bulk}	3530 mol/m^3	Prepared solution
Effective diffusivity (both species)	D	1.2×10^{-9} m^2/s	Effective, lit. values [38,39], §3.2
Surface rate constant	k_s	3.94×10^{-6} m/s	Anchored to measured plateau etch rate (2.5 μm min^{-1})
Bulk Dirichlet offset (Nernst layer)	δ_{BL}	100 μm (loc. min 50)	Fixed, §3.2
Inhibition constant	K_{inh}	6.7×10^{-4} m^3/mol	Fixed (initial estimate, not calibrated)
Intrinsic anisotropy	a_h	0.986	Fixed near-isotropic input, §3.2
AR-closure coefficient	β_p	2.0	Selected in model development, §3.3

openings, and its configuration and boundary conditions are shown in Fig. 3a and b. Because the mask is a line-type geometry that is invariant normal to the cross-section, the two-dimensional approximation is valid at the line center. Three-dimensional effects at the line ends and corners are outside the scope of this study. The concentration fields of Eqs. (1)–(3) were solved quasi-steadily on a finite-volume grid masked by φ, and the interface was advanced by the advection of Eq. (6) with periodic re-initialization, following the solution loop in Fig. 3c. The dummy PR was released when the minimum width of the copper supporting it, measured within 60 μm below the PR, fell below 0.3w. Copper fragments that lost contact with the substrate were dissolved, and the copper directly beneath a supported dummy PR was protected from etching from above. The intervals before and after detachment were computed continuously in a single analysis. The simulator was implemented in Python with the NumPy and SciPy libraries.

The parameters were determined and validated as follows. (i) In the numerical verification, the grid dependence of the tail length and of the cross-sectional profile was evaluated by progressively refining the grid spacing. (ii) k_s was anchored to the measured plateau etch rate of the wide opening, 2.5 μm min^{-1}, δ_{BL} was fixed a priori on the Nernst-layer scale, K_{inh} was kept at its initial estimate, and a_h was treated as a fixed near-isotropic input. The only model coefficient chosen by comparison with measured cross-sections is the aspect-ratio closure coefficient β_p, which, together with the protection of the copper beneath a supported dummy PR and the acceptance of a_h, was selected during model development using four conditions, (s, w) = (100, 100), (200, 100), (150, 150), and (150, 200) μm. The common comparison time, a single global readout offset, was fixed on three dummy-free sections only, as described in Section 4.2. The simulated punch-through time of the wide opening, t_{wc} = 175 min, is later than the measured 150 min because the depth-averaged etch rate of the simulated reference plane (1.7 μm min^{-1}) is lower than the measured one (2.0 μm min^{-1}). Because such a rate offset shifts the timeline rather than the geometry, as noted in Section 2.1, the simulated readouts are referenced to simulated events such as t_{wc} rather than to the absolute etch time. (iii) To keep the validation strict, these four conditions were excluded from the holdout set, and the remaining 12 of the 16 comparison conditions, which entered none of these choices, were compared without any parameter adjustment.

The numerical accuracy and the degrees of freedom were verified separately as follows. First, the concentration fields were solved under a quasi-steady assumption. The diffusive relaxation time over the gap width, $\tau_{diff} = s^2/D$, is 8–133 s for s = 100–400 μm, which is far shorter than the interface-motion timescale of tens of minutes and validates the quasi-steady assumption. Second, the grid dependence was examined by reducing the grid spacing from Δx = 4.0 to 3.0 and 2.0 μm. As shown in Fig. S1 and Table S1, the profiles overlap closely, with variations of 2.1% in the tail length and below 0.4% in the residual area, the latter being

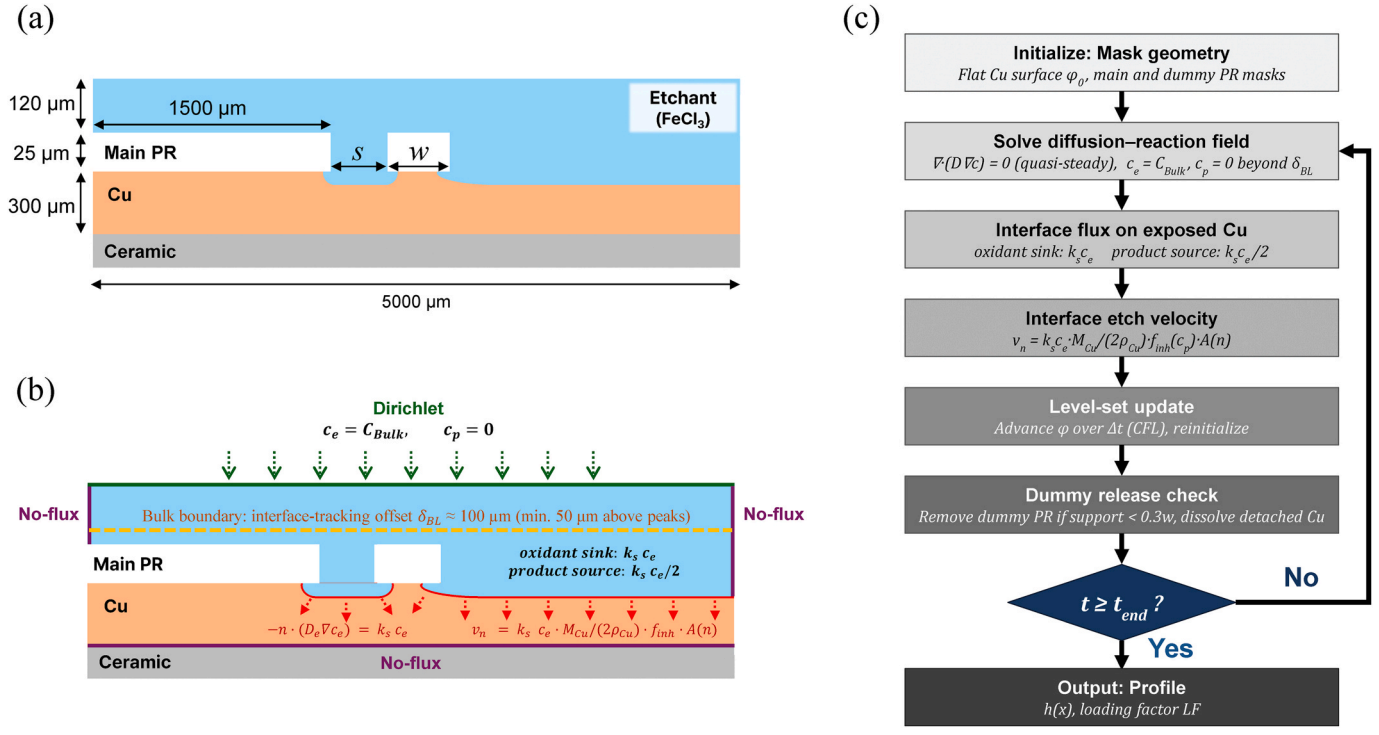


Fig. 3. Simulation setup. (a) Two-dimensional computational domain (5000 × 445 μm), showing $FeCl_3$ etchant (120 μm) over the main PR (25 μm) and Cu (300 μm) on a ceramic base, with opening s and dummy w. (b) Boundary conditions, where liquid beyond the tracking offset δ_{BL} is held at bulk values, the Dirichlet limit of Eq. (2). Exposed Cu follows the first-order flux of Eq. (3) with interface velocity v_n. PR-covered Cu is inert, and all remaining boundaries, including the substrate, are treated as no-flux boundaries. (c) The solution loop, comprising the quasi-steady field solution, interface flux and velocity, level-set update, and dummy release check, is iterated to the target time to obtain $h(x)$ and the loading factor LF.

non-monotonic. Because numerical diffusion on coarser grids smooths the tail toe, the coarser grids lie slightly closer to the measured, rounded toe, and the RMSE against the measurement therefore varies with Δx, as also listed in Table S1. This variation reflects the underprediction of the toe discussed in Section 4.3 rather than a discretization error, whereas the design-relevant quantities, namely the tail length and the residual area, vary only by the amounts given above. The production resolution was $\Delta x = 2.0$ μm, and the smallest opening ($s = 100$ μm) was resolved with 50 cells. Third, the ±20% one-at-a-time local sensitivities under two representative conditions showed a clear ordering in $|S|$, with values of approximately 1.6–1.9 for k_s, 0.7–0.8 for K_{inh}, and 0.1 for β_p. These values refer to the readout at the fixed comparison time. Because k_s and K_{inh} mainly shift the process timeline, changing the punch-through time by 9%–14% and 3%–9%, respectively, the same perturbations read at the protocol time $t_{wc} + \Delta^*$ of each run change L by only $|S| \approx 0.30$–0.34, 0.12–0.28, and 0.10–0.12, as summarized in Fig. S3a and Table S5a. The bulk boundary offset δ_{BL}, which is fixed a priori and not calibrated, was also varied over 50–150 μm. A ±20% change shifts the event-anchored L by −9% and +12% ($|S| \approx 0.54$) and the punch-through time by −9% and +11%, respectively. Over the whole range, the sequence of topological events is unchanged, and the RMSE against the measured section at the protocol time is 7.2–13.4 μm, which lies within the holdout range of 4.5–16.6 μm listed in Table S2, as shown in Fig. S3b and Table S5b. Varying the release fraction from 0.2 to 0.4 shifts the detachment time by 10–26 min and changes L at the comparison time by 4–22 μm and the RMSE by 0.4–1.6 μm. The 16 shape-comparison conditions are all conditions with $w \leq 200$ μm in the production simulation set, not a sample selected after examining the results.

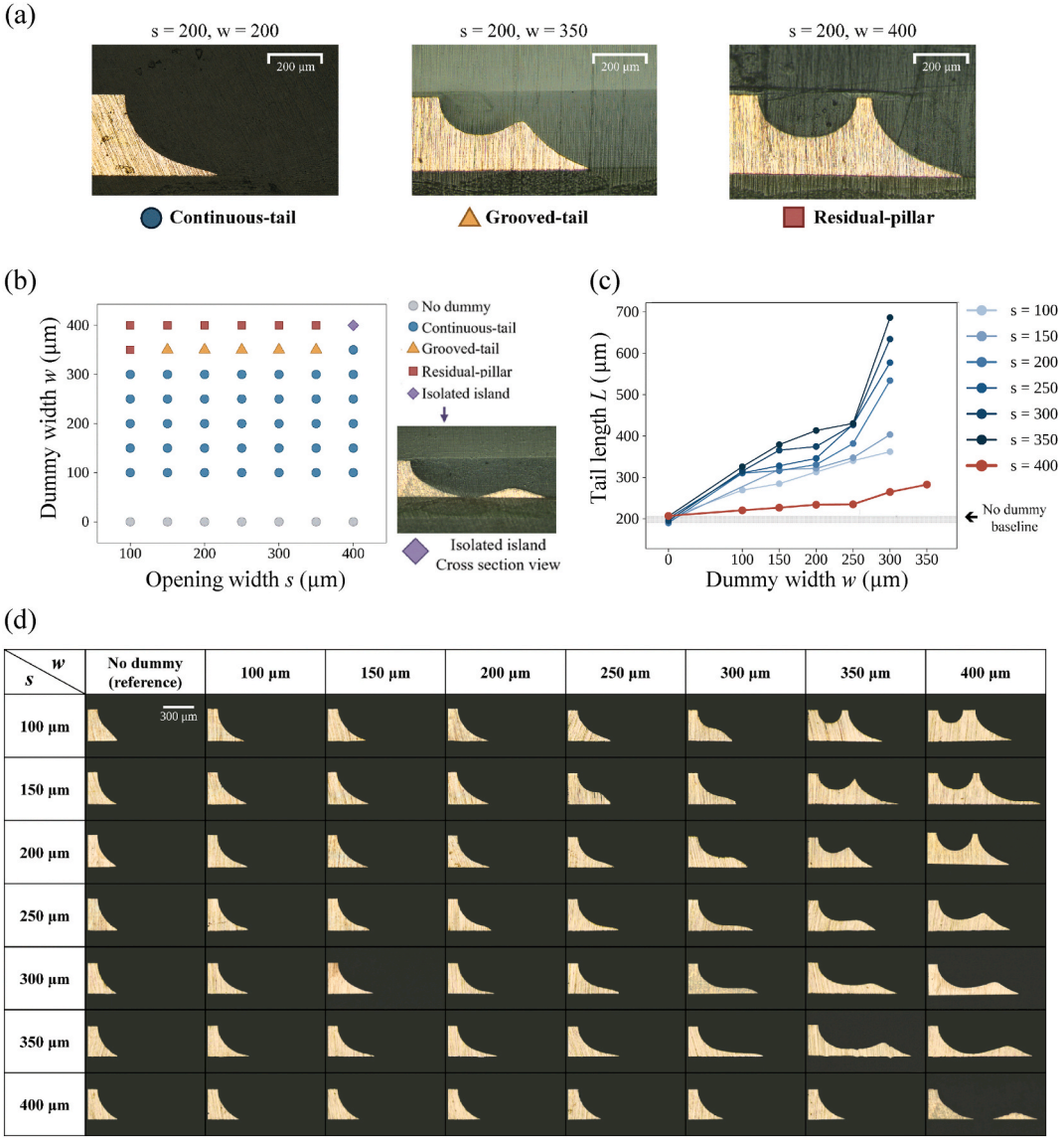


Fig. 4. Regime characterization of the etched edge under dummy patterns. (a) Representative optical-microscope cross-sections at a fixed opening width $s = 200$ μm with increasing dummy width w, illustrating the three morphological regimes: continuous-tail ($w = 200$ μm), grooved-tail ($w = 350$ μm), and residual-pillar ($w = 400$ μm). (b) Regime map over the (s, w) design space. Markers denote the observed regime. The isolated-island regime occurs only at the widest combination ($s = w = 400$ μm) and is shown in the inset. (c) Measured edge-tail length L versus dummy width w, grouped by opening width s. L increases with w at narrow-to-moderate openings, whereas at the widest opening ($s = 400$ μm, red) it remains near the no-dummy baseline (gray band). (d) Optical-microscope cross-sections of all 49 (s, w) combinations and of the seven dummy-free references (rows: opening width s, columns: dummy width w), shown at the same magnification. The scale bar (300 μm) equals the initial copper thickness.

4. Results and discussion

4.1. Experimental regime map

As shown in Fig. 4, the 56 OM cross-sections are digitized from the 49 (w, s) combinations and classified by opening clearance, dummy detachment, and residual structures, dividing the design space into the three morphology regimes illustrated in Fig. 4a and mapped in Fig. 4b. The first is the continuous-tail regime, in which the opening clears normally and the dummy fully detaches and is removed, forming a single continuous tail. Conditions with dummy widths below the groove onset ($w < w_g \approx$ 300–350 μm) belong to this regime. The second is the groove regime, $w_g \lesssim w < w*$, in which the dummy detaches, but its large width imprints the gap etch delay onto the profile, forming a tail containing a U-shaped groove. The third is the residual-pillar regime, $w > w*$, in which the opening etch reaches the substrate before detachment, leaving the dummy-site copper as a pillar. In the measurement set of Fig. 4d, a single continuous tail was maintained up to $w = 300$ μm at all s. Grooves appeared at $w = 350$ μm ($s = 150$–350 μm), giving $w_g \approx$ 300–350 μm. Pillar retention, indicating failure of detachment itself, was observed at $w = 350$ μm ($s = 100$ μm) and $w = 400$ μm ($s = 100$–350 μm), yielding $w^* \approx$ 350–400 μm. Pillar retention was identified when the residual apex protruded above the adjacent tail envelope with its base reaching the substrate. Low bumps that were absorbed into the tail slope were counted as successful detachment. At the widest combination of $s = w = 400$ μm, the residual copper remains as an isolated island, consistent with the decoupling behavior discussed in Section 4.4. The location of this boundary is analyzed in Section 4.7 by a race model between the undercut and the vertical front that includes over-etching.

Within the continuous-tail regime, the tail length L varied monotonically and reproducibly with the dummy and gap dimensions. At fixed s, L increases with w, except that at the widest gap, $s = 400$ μm, the dummy decouples from the main edge and L stays close to the dummy-free reference band shown in Fig. 4c, far below the other gaps. Thus, loading-based shape control holds within a window bounded by the process-resolution limit and w^*. All subsequent analyses targeted this regime, with the residual-pillar regime discussed in Section 4.7 and the sample sizes stated per analysis. The design window used for the design equations is the part of this regime in which Eq. (9) is validated, namely $w \leq 200$ μm and $s \leq 350$ μm, as established in Section 4.4.

4.2. Validation of the simulator against measured cross-sections

This section validates the model at three levels under the model-development and holdout structure described in Section 3.3. All predictions below were obtained with the parameter set and model choices fixed in Section 3.3, and no parameter was adjusted to the holdout conditions. The first level is the shape evolution process. The measured intermediate-time cross-sections of the representative condition shown in Fig. 5a, taken between 30 min and 2.5 h from a separate specimen at each time point, show (i) initially independent etching of the individual openings, (ii) merging of the undercuts beneath the dummy followed by detachment, (iii) a transition of the residual copper from a pillar to a mound after detachment, and (iv) absorption and disappearance of the mound into the tail. The simulation reproduced the occurrence and the order of these topological events, and (ii) and (iii) are intervals that moving-boundary techniques cannot reach. The absolute height of the residual shape, tracked in Fig. 5b, was underpredicted because of the transport limitation discussed later, so the quantitative shape validation was performed on the final cross-sections.

Second, the final cross-sectional geometry is reproduced. Over the 16 comparison conditions with $w \leq 200$ μm, the cross-section RMSE between the simulated final profiles and the measured $h(x)$ had a median of 11.0 μm and a range of 4.5–16.9 μm, corresponding to 1.5%–5.6% of the copper thickness. Over the 12 holdout conditions alone, the median was 10.2 μm and the range 4.5–16.6 μm, and excluding the three $s =$ 400 μm holdout conditions, at which the dummy decouples, the median was 11.7 μm. The overlays for all conditions and per-condition values are presented in Fig. S2 and Table S2. The comparison time is common to all conditions, $t = 230$ min, defined as the simulated punch-through time $t_{wc} = 175$ min plus an offset $\Delta^* = 55$ min that minimizes the tail-length mismatch of three dummy-free sections ($s = 100$, 250, and 400 μm, mean absolute deviation 3.3 μm), so no per-condition time was selected. The deviations were confined to the shallow tail-toe interval, and the pointwise deviations on the steep wall were a geometric effect of a small horizontal front offset. The gentle taper beneath the main PR was formed by a nearly isotropic lateral undercut, with $a_h \approx 0.986$, and was reproduced without any additional interfacial mechanism. In summary,

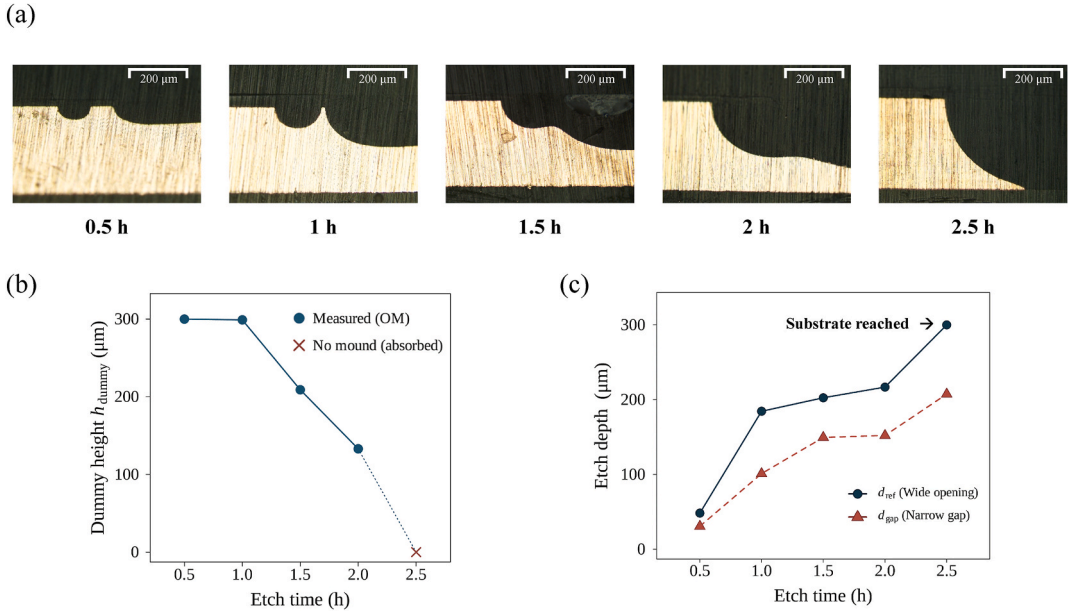


Fig. 5. (a) Measured evolution of the etched edge from optical cross-sections over 0.5–2.5 h, each time point from a separate specimen. (b) Residual-dummy peak height versus etch time, tracking the mound apex. (c) Etch-depth histories of the narrow gap and the wide opening from the same five sections, presented as process data rather than validation data.

the model reproduces the occurrence and order of the four topological events and the final cross-section to within 1.5%–5.6% of the copper thickness, with the height of the residual mound after detachment as the only systematic deviation.

Third, we state the scope of the validation explicitly. The absolute prediction of the tail length L was not included in the validation scope, because a purely diffusive transport model underpredicts the low residual mound that remains after dummy detachment, as analyzed at the end of Section 4.3. The simulation is relied on only for the ordering of the loading suppression at a fixed s, which follows the ordering of the measured L, as shown in Section 4.4. Because the tail apex retracts after the residual copper is absorbed, the simulated tail length is non-monotonic in time, and the relative loading response was therefore read at $t = 185$ min, the first saved time at which every condition shown is past its own punch-through and before the tail collapse. This readout time was fixed by an event internal to the simulation, and the ordering is unchanged over 185–200 min. At this readout, the tail terminus of the simulated profiles moves outward in Fig. 6a, and Fig. 6b shows that L/L_0 increases monotonically with the dummy width w in both the measurements and the simulation, which confirms that the model captures the loading-driven tail response at the level of the trend. In this division of roles, Eq. (9) does not correct the simulation but replaces it for the absolute magnitude of L, whereas the simulation supplies the mechanism, namely the loading factor analyzed in Section 4.3, together with the ordering of the loading response.

4.3. Concentration fields and quantification of the loading effect

The concentration fields of the reactive species, which cannot be measured experimentally, were extracted from the validated simulator. Fig. 7a and b show the oxidant concentration in the gap and in the wide opening for $s = 100$–400 μm, and Fig. 8a shows the oxidant and product concentrations along the copper front. In the wide opening, the oxidant at the reacting floor remains at about 0.75 of the bulk value, and the product is discharged smoothly, so etching proceeds rapidly. Inside the narrow gap, oxidant depletion and product accumulation superimpose and distinctly suppress the local etch rate, consistent with the measured lag of the gap depth in Fig. 5c. This is the loading effect at the level of the concentration field, and it shows that the product supersaturation in cavities reported by Georgiadou and Alkire can be induced at selected positions with a mask design element.

To use the suppression in the concentration field for the design, it must be compressed into a scalar metric. To this end, the punch-through time t_{wc} at which the vertical front of the wide opening reaches the substrate was taken as the evaluation reference, because it is a physical event independent of the mask geometry. The loading factor LF is defined as the ratio of the etch depth d_{gap} in the narrow gap to the etch depth d_{ref} in the bulk-exposed reference plane, as illustrated in Fig. 8b. This depth ratio equals the time-averaged ratio of the etch rates. The evaluation time was fixed at t_{wc} because LF saturates to 1 after punch-through, as shown in Fig. 7c, reaching 1.00 in all conditions within 60 min, and the cross-condition information is then lost.

$$LF = \frac{d_{gap}}{d_{ref}} \tag{7}$$

By definition, $(1 - LF)$ is the fraction of suppression due to loading. Fig. 8 shows the local concentration and etch-rate distributions together with the LF extraction, and Fig. 9a and b show how $(1 - LF)$ varies with s and w, respectively. $(1 - LF)$ increased monotonically as s narrowed and as w widened. Physically, the former reflects the constriction of the supply passage, whereas the latter reflects the increase in the reaction load that the passage must serve, and these distinct mass-transfer roles motivate the non-dimensionalization presented in the next section.

Although the open regions and the main edge were reproduced quantitatively, the low residual mound in the stagnant zone after the disappearance of the dummy was systematically underpredicted, and adjustments of the diffusive transport failed to correct this deficit. The responsible mechanism must be selective with respect to the opening width and must preserve information on the initial trench geometry, and neither property is present in an isotropic diffusion process. Two candidates meet these criteria. The first is threshold-type salt-film precipitation, because the reconstructed product concentration deep in the gap exceeds the reported threshold of about 1 M, and such gate-type blocking cannot be captured by the smooth inhibition of Eq. (5). The second is flow-coupled transport, in which the density and viscosity changes induced by the product are coupled with the recirculation vortex in the cavity. This deficit does not affect Eq. (8). LF is the ratio of two depths taken from the same field, so a common amplitude bias cancels to leading order, and the claim concerns the exponent structure, which is supported by the consistency with (1, 1) and by the ordering correspondence at fixed s described in Section 4.4.

4.4. Dimensionless loading law

The three lengths (d, s, w) yield two independent dimensionless groups according to the Buckingham π theorem, namely the aspect ratio

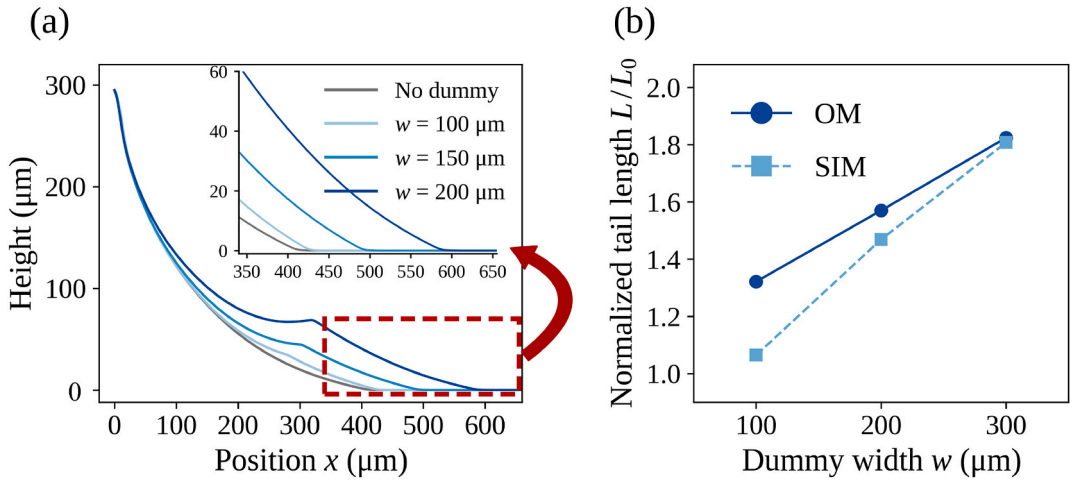


Fig. 6. Simulated and measured edge-tail elongation with increasing dummy width w (opening width $s = 100$ μm). (a) Simulated cross-sectional profiles at $t = 185$ min, shortly after punch-through and before the tail collapse in every cell, for the no-dummy reference and $w = 100$, 150, and 200 μm. The inset magnifies the tail-end region, showing that the tail terminus extends monotonically with w. (b) Tail length normalized by the no-dummy reference, L/L_0, at $w = 100$, 200, and 300 μm for optical microscopy measurements (OM) and simulation (SIM, at $t = 185$ min). Both increase monotonically with w.

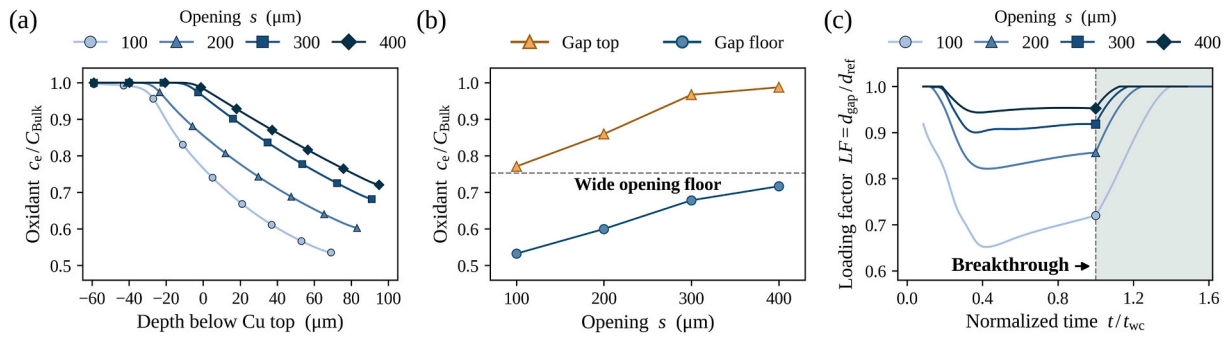


Fig. 7. Origin of the loading effect from local oxidant depletion in the gap between the dummy and the main PR. (a) Simulated oxidant concentration at the etch front, c_e/C_{Bulk}, versus depth below the Cu top surface for $s = 100$–400 μm at $w = 200$ μm and $t = 60$ min, the last saved time before dummy lift-off in all conditions. Narrower openings show stronger depletion. (b) Oxidant concentration at the gap top (inlet) and at the gap floor versus s. Both increase with s, and the gap floor remains well below the wide-opening reference shown by the dashed line, so the depletion is localized in the confined gap. (c) Loading factor $LF = d_{gap}/d_{ref}$ versus normalized etch time t/t_{wc} for $s = 100$–400 μm. LF drops as the confined region lags and recovers once the gap opens, shown by the shaded region with $t/t_{wc} > 1$. A smaller s produces a deeper and more persistent lag. Markers indicate LF at t_{wc}, the value used in Eq. (7).

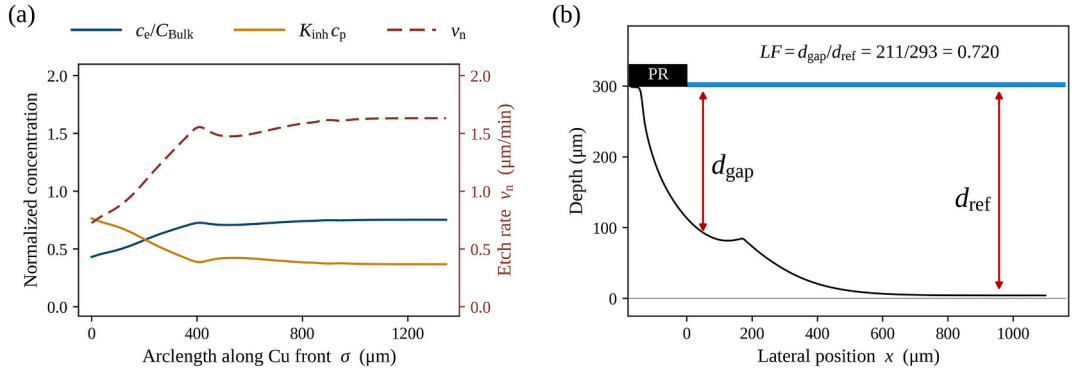


Fig. 8. Extraction of the loading factor for $s = 100$ μm and $w = 200$ μm at $t = t_{wc}$. (a) Local concentration and etch-rate profiles along the copper surface. (b) Definition of the gap and reference etch depths in Eq. (7).

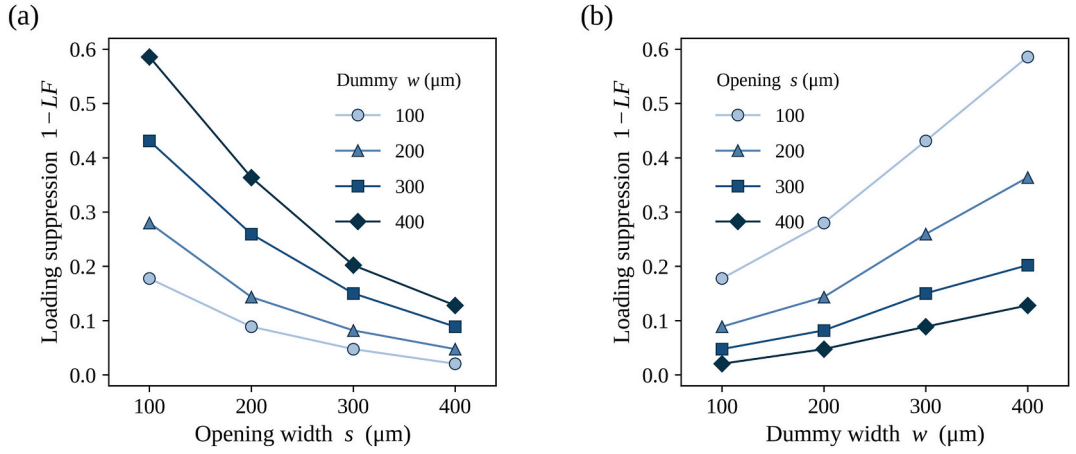


Fig. 9. Loading suppression ($1 - LF$) over the simulated conditions. (a) ($1 - LF$) versus opening width s, grouped by dummy width w. Suppression decreases as the supply channel widens. (b) The same data versus dummy width w, grouped by s. Suppression increases with the reaction load imposed by the dummy coverage.

d/s and the coverage ratio w/d. The former represents the supply constriction, and the latter represents the reaction load. Physically, d/s lengthens the diffusion path through the gap and thus sets how strongly the oxidant is depleted at the gap floor, whereas w/d sets the amount of copper that must be dissolved through the same passage. Together, they fix the local etch-rate suppression that delays the gap front and elongates the merged edge. Regressing ($1 - LF$) from the 28 simulation runs that satisfy the pre-specified criteria of normal completion, punch-through, and $w > 0$ as a power law of the two groups, by nonlinear least squares on the untransformed ($1 - LF$), yields Eq. (8). Because LF is a transport quantity that is independent of the morphology regime, the sample includes all valid runs without regime filtering.

$$1 - LF = 0.154 \cdot \left(\frac{d}{s}\right)^{0.98} \cdot \left(\frac{w}{d}\right)^{1.11} \tag{8}$$

As shown in Fig. 10a, the fit gives $R^2 = 0.97$ with 28 points

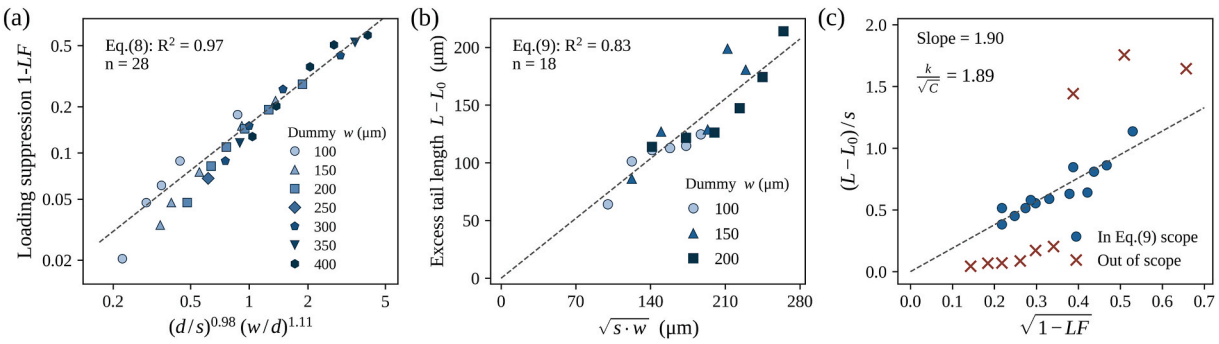


Fig. 10. (a) Collapse of the loading suppression onto the dimensionless law of Eq. (8) over all valid conditions ($R^2 = 0.97$, $n = 28$). (b) Direct experimental collapse of the measured excess tail length $L - L_0$ onto the mask-geometry composite $\sqrt{s \cdot w}$, Eq. (9) ($R^2 = 0.83$, $n = 18$), bypassing the simulation entirely. (c) Combined-law consistency, showing $(L - L_0)/s$ versus $\sqrt{1 - LF}$ within the validity range of Eq. (9), where the collapse slope (1.90) agrees with the algebraic prediction $k/\sqrt{C} = 1.89$ (consistency check, not independent validation). Open crosses mark out-of-scope conditions ($w \geq 250$ μm or $s = 400$ μm).

supporting the three parameters. Because d is fixed at 300 μm in all runs, the present data do not test the thickness dependence of Eq. (8), and for unit exponents the two groups combine into w/s. When the narrow gap is approximated as a quasi-steady one-dimensional diffusion channel, the channel resistance scales with d/s and the reaction flux it serves scales with w/d, so $(1 - LF) \propto (d/s)^1 (w/d)^1$ is predicted to leading order. The exponents in Eq. (8) were obtained by free regression and were not imposed. The regressed values of 0.98 and 1.11 lie close to (1, 1), and the case-resampling bootstrap 95% confidence intervals obtained from 5000 replicates, 0.88–1.19 for d/s and 0.96–1.34 for w/d, contain the unit exponents, as listed in Table S4. The closeness to (1, 1) is therefore reported as a consistency check with the one-dimensional channel argument, not as a derivation of Eq. (8) from it. Of the two groups, d/s shares its scale with the aspect-ratio closure of Section 3.2 and is thus internally consistent, whereas the linearity in w/d is an emergent result of the source-sink balance of Eqs. (2) and (3) and was never injected into the closure. Restricting the sample to $w \leq 200$ μm narrows the range of w and shifts the point estimates to 1.14 for d/s and 0.75 for w/d, as listed in Table S4, a consequence of range-restricted estimation. The full-range fit is consistent with the theoretical values within its confidence intervals. The applicable range of Eq. (8) is the regime of Section 4.1 in which the dummy is removed, that is, an open gap with $w < w^*$, and $(1 - LF)$ is a suppression of the local etch rate, not the tail length itself. Equation (8) is not used for the design itself. The design relation, Eq. (9) below, is established directly from the measurements and is independent of the simulation, and the mutual consistency of the two relations is examined at the end of this section. The coefficients of Eq. (8) refer to the agitation condition represented by $\delta_{BL} = 100$ μm. Varying δ_{BL} by ±20% at four corner conditions of the design space preserves the ranking of $(1 - LF)$ across the conditions, but the response to δ_{BL} depends on the condition and, as listed in Table S5c, is weakest at the most strongly loaded condition ($s = 100$ μm, $w = 200$ μm), where the gap resistance already dominates the external boundary layer. The unit exponents should therefore be read as the limit in which the external boundary-layer resistance is small compared with the gap resistance, and transferring Eq. (8) to a different agitation condition requires its coefficients to be redetermined, as noted for spray etching in Section 5.

Finally, a direct relationship exists between loading and geometry. The intuitive expectation is that a stronger suppression yields a longer tail, but the measurements show that the response is asymmetric with respect to the two design variables. At a fixed s, L increases monotonically with w, whereas at a fixed w, L increases for wider gaps. For example, at $w = 200$ μm, $dL/ds = +0.39$ ($r = 0.95$), and $dL/ds > 0$ holds across the design window. This is because the tail length is set by the geometry from which the merged front departs, and the merging zone spans both s and w, so the rate suppression and the front geometry act in opposite directions with respect to s. A design equation for the tail length was therefore established directly from the measurements. Free regression of the measured excess tail length $(L - L_0)/d$ gives exponents of 0.54 for s/d and 0.51 for w/d, with bootstrap 95% CIs of 0.39–0.71 and 0.27–0.68, neither of which is distinguishable from 1/2 ($R^2 = 0.83$, $n = 18$). Constraining both exponents to 1/2 changes R^2 only from 0.829 to 0.826 and yields the final form. Because w and s are continuous factors sampled on a full 7 × 7 factorial grid, these regressions with bootstrap confidence intervals play the role of an analysis of variance (ANOVA) for the present data, in which the exponents quantify the main effect of each mask variable and the multiplicative form captures their interaction. For completeness, and following the ANOVA-based screening of process parameters that is standard practice in materials-processing and machining studies [41,42], a two-way ANOVA of the measured L over the 18 design-window cells in Table S3a confirms that both w ($F(2, 10) = 9.9$, $p = 0.004$) and s ($F(5, 10) = 8.8$, $p = 0.002$) are significant. As listed in Table S3b, the single regressor $\sqrt{s \cdot w}$ accounts for 83% of the total variance, compared with 86% for the additive two-way model with seven degrees of freedom.

$$L = L_0 + 0.74 \cdot \sqrt{s \cdot w} \tag{9}$$

Here, $L_0 = 199.6$ μm is the mean tail length of the seven dummy-free reference specimens, with an SD of 6.6 μm and a range of 189–205 μm. The dimensionless coefficient $k = 0.74$ was determined by origin-constrained regression on the $n = 18$ sample with $w = 100$–200 μm and $s = 100$–350 μm. The residual standard deviation was 16 μm, and freeing the intercept yielded an estimate of −5.7 μm, which is indistinguishable from zero. The specimen-level repeatability sets the measurement floor of this residual. The dummy-free reference yielded an SD of 6.6 μm over seven specimens, and three repeated specimens at the representative loading condition of $w = s = 100$ μm yielded a mean of 267.8 μm with an SD of 4.1 μm and a range of 7.9 μm. The remaining lack-of-fit component of approximately 15 μm obtained by variance decomposition corresponds to 4%–6% of the design-window tail lengths and reflects condition-to-condition deviations that are not captured by the two-variable mask description. The collapse of Eq. (9) is illustrated in Fig. 10b. A geometric-mean form was adopted on the grounds of parsimony. The wide bootstrap intervals of the free exponents indicate that the data are consistent with an equal weighting of the supply passage s and the reaction load w, but do not establish it uniquely. The consistency of Eqs. (8) and (9) is verified at two levels. First, the correlation between L and $(1 - LF)$ pooled over all conditions is only moderate, because $\partial L/\partial s$ and $\partial(1 - LF)/\partial s$ have opposite signs (Spearman $\rho = 0.60$). However, when s is fixed, $(1 - LF)$ follows the ordering of the measured L, with $\rho > 0$ in every computable s group and $\rho = 1.0$ in five of the six groups. Second, the collapse predicted by combining the two equations, $(L - L_0)/s \propto \sqrt{1 - LF}$, shows a slope of 1.90 within the validated range of Eq. (9), as shown in Fig. 10c. This slope agrees to within

1% with the algebraic prediction $k/\sqrt{C} = 1.89$ obtained by idealizing the exponents to the theoretical values (1, 1). This collapse is a mutual consistency check and not an independent validation. As Fig. 4c shows, the dummy decouples at $s = 400$ μm and L stays close to the reference band. The validated range of Eq. (9) is therefore restricted to $s \leq 350$ μm and $w \leq 200$ μm, where the loading coupling is maintained, and including $w = 250$–300 μm degrades the collapse to $R^2 = 0.72$. Within the validated range, Eq. (9) predicts L with a residual SD of 16 μm, or 4%–6% of L. The practical process window is bounded jointly by the resolution limit of the gap, this validated range, and the removability boundary w^* of Section 4.7, and outside these bounds Eq. (9) has not been validated.

4.5. Self-similar tail shape and master-curve collapse

Controlling the tail length alone is insufficient to predict the entire profile. As shown in Fig. 11a and b, normalizing the digitized profiles $h(x)$ of all the conditions with $w \leq 200$ μm by their own L (horizontal) and d (vertical) collapses the profiles at different (w, s) onto a single curve of the normalized position $\xi = x/L$.

$$h(x) = d \cdot f\left(\frac{x}{L}\right) \tag{10}$$

The median deviation after the collapse is approximately 5 μm, which is at the level of the measurement uncertainty. As shown in Fig. 11b, the same normalization applied independently to the simulated profiles collapses them onto a master curve of the same form, so the self-similarity holds on both sides and is not an artifact of the normalization.

The deviation between the two master curves has a median of 14.7 μm over the 16 conditions, which corresponds to 4.9% of the copper thickness and is of the same order as the measured self-collapse scatter of approximately 5 μm. A localized systematic deviation of up to 51 μm occurs in the near-edge interval $\xi \approx 0.035$, and the measured $f(\xi)$ is therefore used directly for the design. The two implications are as follows. First, the dummy pattern controls only the tail length L, and the dimensionless shape $f(\xi)$ is a single function that is independent of the mask geometry within the tested range. The designer therefore sets L with Eq. (9) and reconstructs the entire profile from the master shape $f(\xi)$ of Eq. (10). Second, the edge angle θ_1 ceases to be an independent design variable. Under self-similarity, the contact slope scales as $\tan\theta_1 \approx |f'(\xi)| \cdot (d/L)$, with f' evaluated at the toe, so θ_1 is not a separate control target but a quantity subordinate to the profile aspect ratio d/L. The measured θ_1 distribution in Fig. 11c shifts distinctly toward gentler angles under dummy conditions, with the median decreasing from 33.4° for the dummy-free $n = 7$ to 24.1° for the dummy specimens with $w \leq 200$ μm, $n = 21$ (Mann–Whitney $U = 143$, $p = 2.0 \times 10^{-5}$), where θ_1 is the 50 μm chord slope at the substrate contact point defined in Fig. 2. For the same specimens, the elongation of L was so pronounced that the two groups separated completely ($U = 0$, $p = 1.7 \times 10^{-6}$). The test is rank-based, and its result is unchanged for chord lengths of 30–70 μm. Long and gentle shapes are thus secured simultaneously by a single loading design, and the degrees of freedom of the shape design are reduced to a single quantity, L, which underpins the inverse design presented in the next section.

4.6. Thermo-mechanical implication of the measured edge profiles

To quantify the thermo-mechanical implication of the realized geometry directly for the measured edge profiles, the digitized cross-sections of Section 2.2 were transferred to a two-dimensional, quasi-static thermo-mechanical finite-element model of a Cu/Al_2O_3/Cu stack under generalized plane strain, built with the Solid Mechanics module of COMSOL Multiphysics 6.1. As shown in Fig. 12a, the model is a half model with the symmetry plane at $x = 0$. The top copper layer (300 μm) carries the measured profile of one condition as a closed polygon and ends at the toe at $x = 4.0$ mm. The 96% Al_2O_3 substrate (380 μm) extends 1.0 mm beyond the toe, and the back-side copper (300 μm) is a continuous plate whose edge lies 0.5 mm beyond the toe and 0.5 mm inside the ceramic edge, which reproduces the layer sequence of a patterned DBC card with a continuous back-side metallization. The 0.5 mm offset between the back-side copper edge and the toe was chosen so that the two free-edge stress concentrations do not overlap, because the layout of the back-side copper is known to modify the stress at the top interface [14]. Copper follows a temperature-dependent elastic–plastic model with two-back-stress Chaboche nonlinear kinematic hardening and the parameter set of Dunne and Hayhurst [43], as in previous thermo-mechanical analyses of Al_2O_3-DBC [8,10,44], and Al_2O_3 is linear elastic. The elastic and thermal properties are listed in Table S6a, and the temperature-dependent parameters of copper in Table S6b. The stack is taken as stress-free at 25 °C and is subjected to four −55/150 °C cycles with 15 min ramps and dwells, that is, 1 cycle h^{-1}, as shown in Fig. 12b, following the temperature extremes of JESD22-A104 condition H. The ramp rate is not prescribed by the standard and was set to 13.7 K min^{-1}. The residual stress from the bonding process is not modeled. Because the same assumption applies to every geometry and the indicators are read in the stabilized last cycle, this omission is expected to affect the ratios mainly through the first-cycle transient. The etch morphology itself was characterized on copper foil laminated on FR-4, as described in Section 2.1, and the stack model evaluates the thermo-mechanical implication of that geometry on a DBC card.

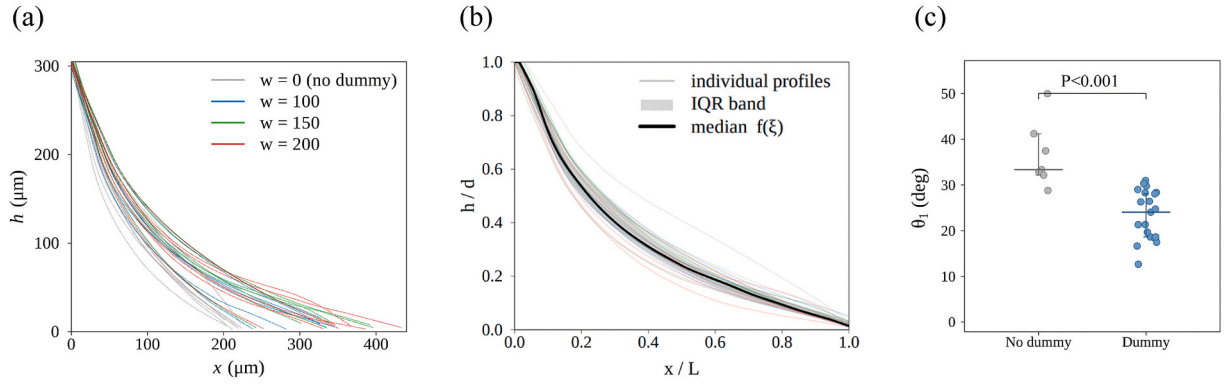


Fig. 11. Self-similarity of the etched edge-tail profile for $w \leq 200$ μm. (a) Measured cross-sectional profiles $h(x)$, aligned at the main-PR corner ($x = 0$, $h = d = 300$ μm) and colored by dummy width w. The conditions differ mainly in the edge-tail length L. (b) Normalization by L in the horizontal and by d in the vertical direction collapses the profiles onto a single master curve, $h/d = f(x/L)$. Thin lines represent individual profiles, the shaded band indicates the interquartile range, and the thick line denotes the median $f(\xi)$. The dummy pattern thus rescales L while leaving $f(\xi)$ invariant. (c) Toe angle θ_1 for the no-dummy specimens ($w = 0$, $n = 7$) and the dummy specimens ($w \leq 200$ μm, $n = 21$). Bars represent group medians, and whiskers indicate bootstrap 95% CIs. Dummy patterns shift θ_1 toward gentler values (Mann–Whitney $p = 2.0 \times 10^{-5}$, $U = 143$).

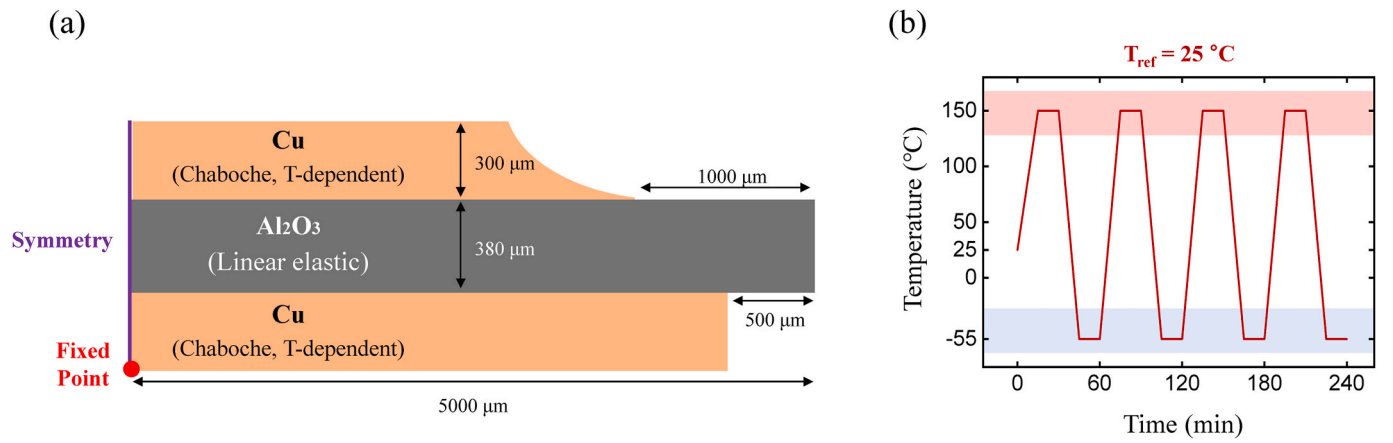


Fig. 12. Thermo-mechanical finite-element model of the DBC cross-section (schematic, not to scale). (a) Two-dimensional generalized-plane-strain half model with the symmetry plane at $x = 0$ and the lower-left corner of the back-side copper fixed. The top copper (300 μm) carries the measured edge profile of each condition and ends at the toe at $x = 4.0$ mm. The Al_2O_3 substrate (380 μm, 5.0 mm wide) extends 1.0 mm beyond the toe, and the back-side copper (300 μm) is a continuous plate whose edge lies 0.5 mm beyond the toe and 0.5 mm inside the ceramic edge. Copper follows a temperature-dependent Chaboche kinematic-hardening model, and Al_2O_3 is linear elastic, with the properties listed in Table S6. (b) Thermal loading, stress-free at $T_{ref} = 25$ °C, with four −55/150 °C cycles of 15 min ramps and dwells according to JESD22-A104 condition H.

Two indicators were extracted from the last cycle along lines 2 μm above and below the copper–ceramic interface, namely the equivalent plastic strain accumulated per cycle in the copper, $\Delta\varepsilon_p$, and the maximum first principal stress in the ceramic, σ_1. Because the field at the toe is singular, each indicator was averaged over a band of the interface measured from the toe, a toe band from 0 to 20 μm and a far band from 50 to 100 μm. The toe band follows the local wedge angle θ_1 of Section 2.2, with $r = 0.97$–0.98 over the 18 design-window cells, and the far band follows the tail length L, with $r = -0.88$ for $\Delta\varepsilon_p$ and -0.67 for σ_1. The two bands are therefore reported separately, as shown in Fig. S4. This division is consistent with the recent finding that the local strain energy density at the copper edge decreases with the notch opening angle [15]. The per-cycle $\Delta\varepsilon_p$ of the third and fourth cycles agreed to four significant digits, so the response had stabilized without ratcheting. As listed in Table S8, the far band changed by less than 1% between the three mesh levels and by less than 4% when the edge of the back-side copper was moved from 0.5 mm to 1.0 mm beyond the toe, that is, to the ceramic edge. Placing the back-side copper edge directly under the toe lowered the indicators by 27%–51% because the two free-edge concentrations then interact, and this configuration was not used. All indicators are normalized by the mean of the seven dummy-free reference profiles listed in Table S7. For these references, the far-band $\Delta\varepsilon_p$ and the toe-band σ_1 scatter by 11% and 10% (one standard deviation), whereas the toe-band $\Delta\varepsilon_p$ scatters by 59% because θ_1 varies between specimens even without a dummy.

Fig. 13 summarizes the result for the 18 cells of the design window ($w \le 200$ μm, $s \le 350$ μm). Every cell lies below the reference in both indicators. The far-band $\Delta\varepsilon_p$ is 0.44–0.73 of the reference mean and decreases with L, and the toe-band σ_1 is 0.49–0.84 of the reference mean, as listed in Table S7. For the fatigue life of the copper, we used the expression that Xu et al. [8] applied to Al_2O_3-DBC under the same −55/150 °C, 1 h cycle. It is the unified expression of Xue for extremely-low-cycle fatigue [45], which has also been used for Al_2O_3-DBC by Dong et al. [44] and for Si_3N_4-AMB by Li et al. [17] and which remains valid when the life falls below about 100 cycles, where the Coffin–Manson law fails:

$$N_f = \frac{1}{2}\left[\frac{e^{\lambda} - 1}{e^{\lambda\varepsilon_d/\varepsilon_f} - 1}\right]^m \tag{11}$$

where ε_d is the equivalent plastic distortion, that is, the equivalent plastic strain range of one cycle, evaluated here as the band-averaged $\Delta\varepsilon_p$, ε_f is the plastic strain at fracture, and $m = 1.56$ and $\lambda = 1.55$ are the constants of annealed OFHC copper [8]. For the far-band strains of the present profiles (2–5×10^{-3}), $\lambda\varepsilon_d/\varepsilon_f \ll 1$, so the bracket reduces to $(e^{\lambda} - 1)\varepsilon_f/(\lambda\varepsilon_d)$. Equation (11) then takes the Coffin–Manson form $N_f \propto$

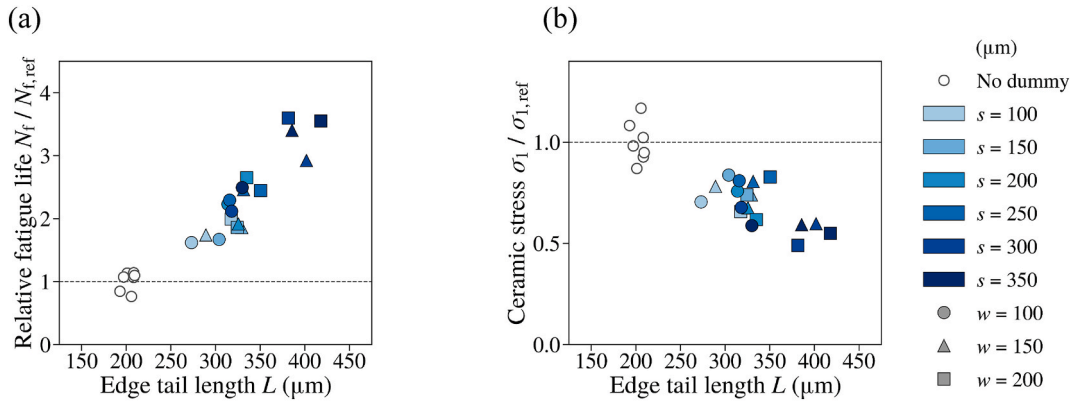


Fig. 13. Thermo-mechanical implication of the measured edge profiles for the 18 cells of the design window versus the tail length L. (a) Relative fatigue life of the copper from Eq. (12) with $m = 1.56$, based on the far-band equivalent plastic strain per cycle. (b) Toe-band maximum first principal stress in the ceramic relative to the reference. Open circles denote the seven dummy-free reference profiles, each normalized by their mean, and the dashed line marks the reference mean. The color indicates the gap s, and the symbol indicates the dummy width w. The values are reference-normalized finite-element estimates, not measured lifetimes.

ε_d^{-m}, with an exponent of $-1/m \approx -0.64$ in the usual notation, and the ratio of two geometries under identical loading becomes independent of ε_f.

$$\frac{N_f}{N_{f,ref}} = \left(\frac{\Delta\varepsilon_p}{\Delta\varepsilon_{p,ref}}\right)^{-m} \tag{12}$$

which yields a relative fatigue life of 1.6–3.6 for the design window that increases with the tail length, as shown in Fig. 13a, and the ratio changes by less than 1% for ε_f between 0.3 and 2.0. The same combination of the Chaboche model and Eq. (11) with these constants predicted about 48 and 136 cycles for a conventional and a ladder-shaped Al_2O_3-DBC under the same −55/150 °C, 1 h cycle, against about 41 and 122 cycles measured on ten substrates each [8], that is, a predicted life ratio of 2.8 against a measured ratio of 3.0. The relative estimates of Fig. 13a are of the same order. A 0.5 mm edge tail that halved the computed plastic strain more than doubled the measured life [10], and the far-band strain ratios of 0.44–0.73 found here are of the same order. Xu et al. evaluated the maximum plastic strain, which lies at the edge corner of the copper, so this benchmark supports the modeling chain but not the choice of band. The far band was used here because the toe band lies at the resolution limit of the OM profiles. The toe-band ratios of 0.12–0.46 would give larger life ratios, so the far-band estimate is the more conservative of the two. The design window lowers the toe-band σ_1 from about 300 MPa for the references to 145–250 MPa, as shown in Fig. 13b. The five cells outside the design window listed in Table S7 behave differently. The three cells with $s = 400$ μm show only a small benefit in the far band, 0.74–0.93, because the dummy decouples at this gap, and the cell with $s = 100$ μm and $w = 300$ μm shows a penalty of 1.23 at the toe because its θ_1 of 43° exceeds the reference mean. The cell with $s = 250$ μm and $w = 300$ μm shows the largest benefit, 0.36 in the far band, but its tail length lies outside the validated range of Eq. (9), so it cannot be designed with the present equations and is not a design target. The edge indicators are defined only once the field copper has been removed ($t \geq t_{wc}$), because no free edge exists before punch-through, as seen in Fig. 5a, and the design target of Section 4.7 is therefore the post-detachment tail.

These values are reference-normalized estimates and not lifetimes. The fatigue constants of Eq. (11) are those of annealed OFHC copper [8] rather than values fitted to the present copper, the copper is a rolled foil laminate rather than the recrystallized copper of a DBC card, the model is two-dimensional and represents a straight edge rather than a pattern corner, and the toe band lies at the resolution limit of the OM cross-sections, as its 59% scatter among the reference profiles shows. Thermal cycling tests were not performed on the present geometries, because the etched specimens are copper foil on FR-4, whose in-plane thermal expansion is close to that of copper, and a meaningful test requires ceramic DBC coupons patterned with the present masks. The modeling chain itself was benchmarked against thermal cycling tests under the same protocol in Ref. [8]. The analysis therefore ranks the measured edge geometries under identical assumptions and quantifies the direction and the order of the benefit, but it does not predict the absolute lifetime of a DBC card.

4.7. Design procedure and the dummy-removability boundary

The results were integrated into an inverse design procedure in which the loading is the only control variable. (1) Set the target tail length L from the reliability requirements by using the relative fatigue-life estimate of Section 4.6, which increases continuously with L within the design window, as shown in Fig. 13a. (2) Using the master shape $f(\xi)$ of Eq. (10), identify θ_1 and the profile that correspond to L. (3) Invert the measurement-based design equation, Eq. (9), to obtain the (w, s) combinations that realize L. From $L - L_0 = 0.74 \cdot \sqrt{s \cdot w}$, the target product $s \cdot w$ is fixed. Because one equation contains two design variables, a unique solution requires an additional constraint, such as fixing the dummy width or imposing a minimum gap width. Within the design window, Eq. (9) gives tail lengths of about 270–400 μm. The 0.5 mm tail examined in Ref. [10] is a tested point rather than a threshold, and as shown in Section 4.6 and Fig. 13, the mechanical benefit of blunting the corner singularity grows continuously with L and with the accompanying reduction of θ_1. The achievable range therefore remains directly relevant to the reliability motivation. (4) Check whether the selected (w, s) lies inside the design window, meaning that the gap is at or above the process resolution limit and that $w < w^*$. The final gate of the procedure, w^*, is the boundary of dummy removability, which is derived directly from the race between the two fronts. The undercut u beneath the dummy, taken as half of the loss of the dummy copper width at the original surface, $u = (w - w_{top})/2$, advances in proportion to the depth z of the wide opening, $u \approx \eta_{eff} \cdot z$, in both the simulation and the measurement. The effective undercut ratio η_{eff}, which includes both the intrinsic anisotropy and the loading-induced limitation of the lateral supply, was computed by origin-constrained u-z regression on pre-detachment simulation snapshots of the 17 conditions with $w \leq 250$ μm, giving a median of 0.713 and a between-condition SD of 0.040, with a per-run R^2 of 0.95–0.998. This value lies within the admissible range of 0.28–0.74 extracted from the measured cross-sections, and neither the detachment time nor the measured boundary enters its computation. The per-s medians cluster at 0.68–0.74, whereas the median decreases from about 0.75 to 0.67 as w grows from 100 to 250 μm, so applying $\eta_{eff} = 0.713$ at $w \approx 428$ μm extrapolates beyond the estimation range and tends to overestimate w^*. The pre-specified estimator was nevertheless kept, and w^* is treated as a single s-independent boundary with a tolerance band of ±24 μm propagated from the between-condition SD of η_{eff}. Detachment occurs only if the two undercuts meet, that is, when $2u \geq w$, before etching is completed. Because the lateral undercut continues to advance during over-etching after the front reaches the substrate ($z = d$), letting f_{OE} denote the over-etch fraction and $z_{end} = (1 + f_{OE}) \cdot d$ the total advance in terms of the vertical front, the detachability condition becomes

$$w < w* = 2\eta_{eff} \cdot (1 + f_{OE}) \cdot d. \tag{13}$$

Because the present process has no over-etch period ($f_{OE} = 0$) and its total etching time of 2.5 h coincides with the substrate arrival time t_{wc} of the wide opening, the boundary simplifies to $w^* = 2\eta_{eff} \cdot d$. Substituting the simulated η_{eff} gives $w^* = 2 \times 0.713 \times 300 \approx 428 \pm 24$ μm, with the uncertainty propagated entirely from the η_{eff} scatter. In the measured regime map, pillar retention appears only at $w = 350$ μm ($s = 100$ μm) and $w = 400$ μm ($s = 100$–350 μm), providing a measured boundary of $w^* \approx 350$–400 μm (1.2–1.3d). The prediction of 428 ± 24 μm, obtained with no parameter tuned to the boundary, lies about 30 μm, less than one mask step (50 μm), above the upper end of the measured bracket. The direct simulations show the same offset: dummies of $w = 400$ μm detach before punch-through for $s \geq 150$ μm but not for $s = 100$ μm, whereas the measured sections retain pillars at $w = 400$ μm. The simulator therefore places the removability boundary about one mask step too high, consistent with a slightly too fast lateral etch, and the measured bracket of 350–400 μm is used as the removability gate of the design procedure. The measured bracket rests on one specimen per condition, and its width equals the 50 μm grid spacing of the mask. The lower measured boundary at $s = 100$ μm (300–350 μm) is reproduced in direction by the direct simulations and is consistent with the w-dependent decrease in η_{eff}.

In the residual-pillar regime ($w > w^*$), the model predicts the direction of change in the residual amount but systematically underpredicts its amplitude, indicating that the fully transport-limited mass transfer in this regime requires reparameterization. The design procedure is therefore validated only within the design window, and the pillar regime is left for future work.

Table 3 compares the proposed method with existing edge-geometry control techniques from a process perspective. Whereas existing techniques require additional lithography and alignment and obtain the

Table 3
Comparison of edge-profile control approaches for DBC copper patterns.

Approach	Process (steps/ alignment)	Controlled quantity	Profile predictability	Limitation	Basis of profile reproducibility
Edge-tail extension [10]	Single etch, no alignment	Edge-tail length L' (FE parameter)	Empirical (FE)	Tail tested, etch control of the tail not reported	Tail length varied in FE, etch realization not addressed
Dimple structuring [11]	≥2 litho + local etch, alignment	Local recess	Empirical	Extra local etch, hard to realize precisely	Recess depth fixed by separate patterning and local etch
Stepped/ladder edge [8]	Multistep, alignment	Step geometry	Empirical	Multistep, designed tail hard to realize	Step thickness fixed by separate patterning, alignment required
Back-side pattern design [14]	Layout change, no extra step	Back-side copper pattern	FE-based	Relieves stress by layout, edge profile not controlled	Layout fixed by the back-side mask, edge profile not addressed
FE + ML geometry optimization [15]	Not addressed (design study)	Notch angle, dimple geometry	FE surrogate (random forest)	Optimal geometry not linked to a fabrication route	Geometry assumed in FE, etch realization not addressed
This study	**Single etch, no alignment**	Tail length L (θ1 constrained by L)	Quantitative, Eqs. (9), (10) and (13)	**Etch-realized tail,** predicted by Eqs. (9), (10) and (13)	**Mask geometry (*s*, *w*) only,** Eqs. (9) and (10)**, post-detachment tail**

geometry only empirically, the present method predicts and inverts the geometry with quantitative design equations within a single lithography step and a single etch. In more detail, the edge-tail study [10] tested a 0.5 mm tail and varied the tail length in finite-element analysis but did not address how the etch sets the tail geometry. The dimple [11] and stepped or ladder-type [8] designs, whose lifetime benefit has recently been confirmed experimentally with a combined initiation–propagation lifetime model [12], obtain their geometry from a separately patterned copper thickness, so the profile is fixed by an additional lithography and alignment step rather than by the etch itself. More recent design studies have optimized the notch geometry at the copper edge by finite-element and machine-learning search [15] or relieved the interface stress through the layout of the back-side copper [14]. Like [10], they do not address how the edge profile is produced by etching, and their evidence rests mainly on finite-element analysis. Dummy patterns, in turn, have been used in dry and wet etching to equalize the pattern density [23–25], where the loading effect is treated as a uniformity disturbance to be minimized, and the diffusion-reaction models of copper etching [19–22] describe the shape evolution of a single cavity without topology change. The present method differs from all of these in the basis on which the profile is reproduced, which is summarized in the last column of Table 3. The post-detachment tail is a function of the mask geometry (s, w) only, through Eqs. (9) and (10), whereas the pre-detachment groove-and-ridge state is a transient whose residual thickness depends on the etch time. The reproducible design target of this study is therefore the post-detachment tail within the design window.

5. Conclusions

This study converted the loading effect, long regarded as a defect in wet etching, into a design variable that sets the edge-tail geometry through dummy patterns alone. The main conclusions are as follows.

First, the 56 OM cross-sections of all 49 (w, s) combinations divide the design space into continuous-tail, groove, and residual-pillar regimes. Within the design window ($w \leq 200$ μm, $s \leq 350$ μm), bounded by the gap resolution limit and the removability boundary w^*, the tail length varies monotonically and reproducibly with the mask geometry, with a specimen-level repeatability SD of 4–7 μm.

Second, the topology-capable level-set simulator reproduces the sequence of topological events and, without parameter adjustment, the final cross-sections of 12 holdout conditions with a median RMSE of 10.2 μm.

Third, the loading suppression obtained from the simulated fields follows $(1-LF) = 0.154 \cdot \left(\frac{d}{s}\right)^{0.98} \cdot \left(\frac{w}{d}\right)^{1.11}$ ($R^2 = 0.97$, $n = 28$) in terms of the supply constriction d/s and the reaction load w/d, with exponents consistent with the one-dimensional channel prediction (1, 1). The measured tail length follows the mask-only design equation $L = L_0 + 0.74 \cdot \sqrt{s \cdot w}$ $(R^2 = 0.83)$.

Fourth, the measured profiles collapse onto a single master curve $h(x) = d \cdot f(x/L)$ with a median deviation of about 5 μm, so the dummy pattern controls only L while the shape is common to all tested conditions. The removability boundary $w* = 2\eta_{\mathrm{eff}} \cdot d$, predicted without tuning as $w^* = 428 \pm 24$ μm, exceeds the measured 350–400 μm by less than one mask step.

Fifth, transferring the measured profiles to a thermo-mechanical finite-element model of the Cu/Al_2O_3/Cu stack (−55/150 °C cycling) showed that all 18 design-window cells reduce the cyclic plastic strain of the copper to 0.44–0.73 and the toe stress of the ceramic to 0.49–0.84 of the dummy-free reference, a relative fatigue life of 1.6–3.6 from the extremely-low-cycle fatigue expression used for Al_2O_3-DBC. The benefit increases with the tail length.

Sixth, in practical terms, the results provide a mask-only design procedure for the copper edge. A target tail length of about 270–400 μm is converted into a (w, s) pair with Eq. (9), the profile follows from Eq. (10), and the removability is checked with Eq. (13). Because no additional lithography or etching step is required, the procedure can be introduced into industrial DBC patterning through the mask drawing alone, and transfer to other copper thicknesses is expected after recalibration on a dummy-free reference coupon.

The limitations of the present study are stated explicitly. (i) The simulator predicts the topological events, the final cross-section, and the ordering of the loading response, but not the absolute tail length, which is systematically underpredicted after dummy detachment because of a transport mechanism that isotropic diffusion does not resolve, as discussed in Section 4.3. (ii) The etch morphology was characterized on rolled copper foil on FR-4, so a_h should be re-verified on recrystallized DBC copper. (iii) The analysis is two-dimensional at the line center, whereas the stress maximum of real layouts occurs at pattern corners. (iv) The residual-pillar regime is predicted only in direction. (v) The thermo-mechanical benefit rests on a two-dimensional finite-element analysis of the DBC stack whose modeling chain reproduced measured thermal cycling lives of Al_2O_3-DBC in Ref. [8]. The results are relative estimates with literature fatigue constants, not measured lifetimes, and thermal cycling tests on ceramic DBC substrates were not part of this study.

Transfer to production-type spray etching is the main open step. Because agitation enters only through the bulk boundary offset δ_{BL} and the reference-plane etch rate, impinging jets are expected to shift rather than eliminate the design window, since the gap interior remains diffusion controlled, but these parameters must be recalibrated. For industrial substrates and aging $FeCl_3$ baths, a single depth time series on a dummy-free reference coupon suffices to re-anchor k_s and the bulk boundary values of Eq. (2). Thermal cycling tests on ceramic DBC substrates and the determination of the coefficients at other thicknesses and under spray conditions are the next steps toward industrial application. More broadly, a mass-transfer phenomenon so far managed as a defect can be converted into a quantitative design resource.

Data availability statement

Data will be made available on request.

Declaration of competing interest

The authors declare that they have no known competing financial interests or personal relationships that could have appeared to influence the work reported in this paper.

Acknowledgments

This research was supported by the ANCHOR through the Seoul ANCHOR Center, funded by the Ministry of Education (MOE) and the Seoul Metropolitan Government. (2026-ANCHOR-01-027-04), and by the National Research Foundation of Korea (NRF), funded by the Ministry of Science and ICT of Republic of Korea (No. RS-2023-00260527).

Appendix A. Supplementary data

Supplementary data to this article can be found online at https://doi.org/10.1016/j.jmrt.2026.10.134.

References

[1] Reimers J, Dorn-Gomba L, Mak C, Emadi A. Automotive traction inverters: current status and future trends. IEEE Trans Veh Technol 2019;68:3337–50. https://doi.org/10.1109/TVT.2019.2897899.
[2] Wang Y, Dai X, Liu G, Wu Y, Li Y, Jones S. Status and trend of power semiconductor module packaging for electric vehicles. In: Fakhfakh MA, editor. Modeling and simulation for electric vehicle applications. Rijeka: InTech; 2016. p. 23–46. https://doi.org/10.5772/64173.
[3] Khazaka R, Mendizabal L, Henry D, Hanna R. Survey of high-temperature reliability of power electronics packaging components. IEEE Trans Power Electron 2015;30:2456–64. https://doi.org/10.1109/TPEL.2014.2357836.
[4] Mohammed I, Liechti KM. The effect of corner angles in bimaterial structures. Int J Solid Struct 2001;38:4375–94. https://doi.org/10.1016/S0020-7683(00)00389-9.
[5] Akisanya AR, Meng CS. Initiation of fracture at the interface corner of bi-material joints. J Mech Phys Solid 2003;51:27–46. https://doi.org/10.1016/S0022-5096(02)00076-5.
[6] Fu S, Yang Z, Li J. Progress of high strength and high thermal conductivity Si_3N_4 ceramics for power module packaging. J Inorg Mater 2023;38:1117–32. https://doi.org/10.15541/jim20230037.
[7] Schulz-Harder J. Advantages and new development of direct bonded copper substrates. Microelectron Reliab 2003;43:359–65. https://doi.org/10.1016/S0026-2714(02)00343-8.
[8] Xu L, Wang M, Zhou Y, Qian Z, Liu S. An optimal structural design to improve the reliability of Al_2O_3–DBC substrates under thermal cycling. Microelectron Reliab 2016;56:101–8. https://doi.org/10.1016/j.microrel.2015.11.013.
[9] Kim D, Yamamoto Y, Nagao S, Wakasugi N, Chen C, Suganuma K. Measurement of heat dissipation and thermal-stability of power modules on DBC substrates with various ceramics by SiC micro-heater chip system and Ag sinter joining. Micromachines 2019;10:745. https://doi.org/10.3390/mi10110745.
[10] Dong G, Lei G, Chen X, Ngo K, Lu G. Edge tail length effect on reliability of DBC substrates under thermal cycling. Solder Surf Mt Technol 2009;21:10–5. https://doi.org/10.1108/09540910910970367.
[11] Han L, Liang L, Chen D, Zhao Z, Luo F, Kang Y. Modeling and analysis of mesh pattern influences on DBC thermal cycling reliability. Microelectron Reliab 2020;110:113645. https://doi.org/10.1016/j.microrel.2020.113645.
[12] Gaiser P, Klingler M, Wilde J. Lifetime model for the fatigue fracture in Cu/Al_2O_3/Cu composites: experimental validation of a substantial lifetime enhancement by Cu step etching. J Electron Packag 2020;142:021011. https://doi.org/10.1115/1.4046619.
[13] Xu L, Liu S, Wang M, Zhou S. Crack initiation and propagation mechanism of Al_2O_3-DBC substrate during thermal cycling test. Eng Fail Anal 2020;116:104720. https://doi.org/10.1016/j.engfailanal.2020.104720.
[14] Zhang C, Chen C, Zhang Y, Yan Y, Kang Y. A stress-relieved method based on bottom pattern design considering thermal and mechanical behavior of DBC substrate. IEEE Access 2022;10:125735–43. https://doi.org/10.1109/ACCESS.2022.3225657.
[15] D'Andrea D, Sparaino SC, Papaserio M, Orlando S, Babulano GA, Risitano G, et al. Machine learning algorithms for design optimization of ceramic substrates-DBC for power applications using local approaches. Procedia Struct Integr 2026;79:283–90. https://doi.org/10.1016/j.prostr.2025.12.335.
[16] Ngo MC, Miyazaki H, Hirao K, Ohji T, Fukushima M. Stress–strain behavior of Cu on the AMB-Si_3N_4 substrate undergoing thermal cycles via in situ strain measurement. J Am Ceram Soc 2024;107:8415–25. https://doi.org/10.1111/jace.20052.
[17] Li D, Ma Z, Yang H, Xin C, Wang Q. Thermal cycling simulation and fatigue lifetime estimation of Si_3N_4-AMB substrates. Mater Sci Semicond Process 2024;182:108737. https://doi.org/10.1016/j.mssp.2024.108737.
[18] Venkatesh R. Synthesis of CNT fiber with different stacking-made polyester composite via compression mold: mechanical behavior study. J Inst Eng: Series D 2024. https://doi.org/10.1007/s40033-024-00720-w.
[19] Kuiken HK. Etching: a two-dimensional mathematical approach. Proceedings of the Royal Society of London A Mathematical and Physical Sciences 1984;392:199–225. https://doi.org/10.1098/rspa.1984.0029.
[20] Georgiadou M, Alkire R. Anisotropic chemical etching of copper foil: I. Electrochemical studies in acidic $CuCl_2$ solutions. J Electrochem Soc 1993;140:1340–7. https://doi.org/10.1149/1.2220981.
[21] Georgiadou M, Alkire R. Anisotropic chemical etching of copper foil: II. Experimental studies on shape evolution. J Electrochem Soc 1993;140:1348–55. https://doi.org/10.1149/1.2220982.
[22] Georgiadou M, Alkire R. Anisotropic chemical pattern etching of copper foil: III. Mathematical model. J Electrochem Soc 1994;141:679–89. https://doi.org/10.1149/1.2054791.
[23] Coburn JW, Winters HF. Conductance considerations in the reactive ion etching of high aspect ratio features. Appl Phys Lett 1989;55:2730–2. https://doi.org/10.1063/1.101937.
[24] Gottscho RA, Jurgensen CW, Vitkavage DJ. Microscopic uniformity in plasma etching. J Vac Sci Technol B: Microelectronics and Nanometer Structures Processing, Measurement, and Phenomena 1992;10:2133–47. https://doi.org/10.1116/1.586180.
[25] Kiihamäki J, Franssila S. Pattern shape effects and artefacts in deep silicon etching. J Vac Sci Technol A: Vacuum, Surfaces, and Films 1999;17:2280–5. https://doi.org/10.1116/1.581761.
[26] Pilkey WD, Pilkey DF. Peterson's stress concentration factors. third ed. Hoboken, NJ: John Wiley & Sons; 2008.
[27] Bayer CF, Baer E, Waltrich U, Malipaard D, Schletz A. Simulation of the electric field strength in the vicinity of metallization edges on dielectric substrates. IEEE Trans Dielectr Electr Insul 2015;22:257–65. https://doi.org/10.1109/TDEI.2014.004285.
[28] Chanmanwar R, Mohale V, Shinde D, Raut D. Optimization of wet chemical etching for MRR and undercut by substrate orientation. Mater Manuf Process 2026;41:984–95. https://doi.org/10.1080/10426914.2026.2660067.
[29] Allen DM, Almond HJA. Characterisation of aqueous ferric chloride etchants used in industrial photochemical machining. J Mater Process Technol 2004;149:238–45. https://doi.org/10.1016/j.jmatprotec.2004.02.044.
[30] Wang Z, Che J, Ye C. Application of ferric chloride both as oxidant and complexant to enhance the dissolution of metallic copper. Hydrometallurgy 2010;105:69–74. https://doi.org/10.1016/j.hydromet.2010.07.013.
[31] Hu HH, Patankar NA, Zhu MY. Direct numerical simulations of fluid–solid systems using the arbitrary lagrangian–eulerian technique. J Comput Phys 2001;169:427–62. https://doi.org/10.1006/jcph.2000.6592.
[32] Sethian JA. Level set methods and fast marching methods: evolving interfaces in computational geometry, fluid mechanics. Computer vision, and materials science. second ed. Cambridge: Cambridge University Press; 1999.
[33] Osher S, Sethian JA. Fronts propagating with curvature-dependent speed: Algorithms based on hamilton-jacobi formulations. J Comput Phys 1988;79:12–49. https://doi.org/10.1016/0021-9991(88)90002-2.
[34] Adalsteinsson D, Sethian JA. A level set approach to a unified model for etching, deposition, and lithography II: three-dimensional simulations. J Comput Phys 1995;122:348–66. https://doi.org/10.1006/jcph.1995.1221.
[35] Radjenović B, Radmilović-Radjenović M, Mitrić M. Level set approach to anisotropic wet etching of silicon. Sensors 2010;10:4950–67. https://doi.org/10.3390/s100504950.
[36] Mai W, Soghrati S, Buchheit RG. A phase field model for simulating the pitting corrosion. Corros Sci 2016;110:157–66. https://doi.org/10.1016/j.corsci.2016.04.001.
[37] Ansari TQ, Xiao Z, Hu S, Li Y, Luo J-L, Shi S-Q. Phase-field model of pitting corrosion kinetics in metallic materials. npj Comput Mater 2018;4:38. https://doi.org/10.1038/s41524-018-0089-4.
[38] Ribeiro ACF, Esteso MA, Lobo VMM, Valente AJM, Simões SMN, Sobral AJFN, et al. Diffusion coefficients of copper chloride in aqueous solutions at 298.15 K and 310.15 K. J Chem Eng Data 2005;50:1986–90. https://doi.org/10.1021/je050220y.
[39] Vaňýsek P. Ionic conductivity and diffusion at infinite dilution. In: Haynes WM, editor. CRC handbook of chemistry and physics. 96th ed. Boca Raton, FL: CRC Press; 2015. p. 5–98.
[40] Sussman M, Smereka P, Osher S. A level set approach for computing solutions to incompressible two-phase flow. J Comput Phys 1994;114:146–59. https://doi.org/10.1006/jcph.1994.1155.
[41] Venkatesh R. Magnesium alloy and silicon nitrides composite study: synthesis and abrasive water jet machining behavior and optimization. SAE Int J Mater Manuf 2025;18:191–8. https://doi.org/10.4271/05-18-02-0014.
[42] Venkatesh R. Machining parameter optimization and study the turning operation behaviour of hybrid Al/Mg composites. Jordan Journal of Mechanical and Industrial Engineering 2024;18:711–9. https://doi.org/10.59038/jjmie/180407.

[43] Dunne FPE, Hayhurst DR. Continuum damage based constitutive equations for copper under high temperature creep and cyclic plasticity. Proc R Soc London, Ser A 1992;437:545–66. https://doi.org/10.1098/rspa.1992.0079.
[44] Dong G, Chen X, Zhang X, Ngo KDT, Lu G-Q. Thermal fatigue behaviour of Al_2O_3-DBC substrates under high temperature cyclic loading. Solder Surf Mt Technol 2010;22:43–8. https://doi.org/10.1108/09540911011036280.
[45] Xue L. A unified expression for low cycle fatigue and extremely low cycle fatigue and its implication for monotonic loading. Int J Fatig 2008;30:1691–8. https://doi.org/10.1016/j.ijfatigue.2008.03.004.